

Cosmic-ray searches with the MATHUSLA detector



mathusla-experiment.web.cern.ch

Cristiano Alpigiani^a , J. C. Arteaga-Velázquez^{b,*} , Daniela Blanco-Lira^g , Davide Boscherini^c , K. S. Caballero-Mora^d , Paolo Camarri^{e,f} , Roberto Cardarelli^e , Dennis Cazar Ramírezⁱ , Giuseppe Di Sciascio^e , Arturo Fernández Téllez^g , H. J. Lubatti^a , O. G. Morales-Olivares^{d,j} , Piter Amador Paye Mamani^h , David Rivera Rangel^b , Mario Rodríguez-Cahuantzi^g , Rinaldo Santonico^{e,f} , Martin Alfonso Subieta Vázquez^h

^a*University of Washington, Seattle, WA, USA*

^b*Instituto de Física y Matemáticas, Universidad Michoacana, Morelia, Michoacan, Mexico*

^c*Istituto Nazionale di Fisica Nucleare, Sezione di Bologna, Bologna, Italy*

^d*Universidad Autónoma de Chiapas, Tuxtla Gutiérrez, Chiapas, Mexico*

^e*Istituto Nazionale di Fisica Nucleare, Sezione di Roma Tor Vergata, Roma, Italy*

^f*Università degli Studi di Roma Tor Vergata, Roma, Italy*

^g*Benemérita Universidad Autónoma de Puebla, Puebla, Mexico*

^h*Universidad Mayor de San Andrés, La Paz, Bolivia*

ⁱ*Universidad San Francisco de Quito USFQ, Quito, Ecuador*

^j*Escuela Nacional de Ciencias de la Tierra, UNAM, Ciudad de Mexico, Mexico*

**Corresponding author. Email address: juan.arteaga@umich.mx*

ABSTRACT: The performance of the proposed MATHUSLA detector as an instrument for studying the physics of cosmic rays by measuring extensive air showers is presented. The MATHUSLA detector is designed to observe and study the decay of long-lived particles produced at the pp interaction point of the CMS detector at CERN during the HL-LHC data-taking period. The proposed MATHUSLA detector will be composed of many layers of long scintillating bars that cannot measure more than one hit per bar and correctly report the hit coordinate in case of multiple hits. This study shows that adding a layer of RPC detectors with both analogue and digital readout significantly enhances the capabilities of MATHUSLA to measure the local densities and arrival times of charged particles at the front of air showers. We discuss open issues in cosmic-ray physics that the proposed MATHUSLA detector with an additional layer of RPC detectors could address and conclude by comparing with other air-shower facilities that measure cosmic rays in the PeV energy range.

KEYWORDS: MATHUSLA, cosmic rays, multi-messenger astronomy, extensive air showers

Contents

1	Introduction	1
2	A glance at cosmic-ray physics	2
3	The MATHUSLA Detector	4
3.1	Scintillating Detector Planes	5
3.2	Cosmic Rays	6
4	The RPC detector	6
4.1	Introduction	6
4.2	The RPC sub-detector	7
4.3	The RPC front-end electronics	9
4.3.1	Preamplifier	9
4.3.2	Discriminator	11
4.3.3	TDC	12
4.3.4	Trigger and data acquisition	13
4.3.5	Time schedule	15
5	Simulations	16
5.1	Air shower simulations	16
5.2	Simulation of the MATHUSLA detector	17
6	Event reconstruction	18
6.1	Shower core position	18
6.2	Arrival direction of the air shower	21
6.3	Lateral density distribution of EAS	24
7	Selection criteria	25
8	Results	25
8.1	Performance of the RPC	25
8.1.1	Reconstruction efficiency	25
8.1.2	Systematic uncertainties in EAS reconstruction	25
8.1.3	Fraction of hit Big Pads at the RPC layer	28
8.1.4	Maximum density of hit particles at the Big Pads due to EAS events	29
8.1.5	Spatial structure of EAS at the RPC layer	29
8.1.6	Lateral distribution of EAS from the RPC data	31
8.1.7	Potential estimators of the cosmic-ray energy from the RPC data	32
8.1.8	Sensitivity of the lateral shower age to the mass of the cosmic ray	33

8.2	Performance of the scintillating layers	34
8.2.1	Reconstruction efficiency	34
8.2.2	Systematic uncertainties in EAS reconstruction	35
8.3	Fraction of detector hits per layer	37
8.4	Saturation of the scintillation detector layers of MATHUSLA	38
8.5	Muon bundles in MATHUSLA	39
8.5.1	Events from highly inclined EAS	39
8.5.2	Events in tandem with the CMS detector	41
8.5.3	Searching for exotic shower events with MATHUSLA	42
9	Discussion	44
9.1	Comparison with other EAS detectors	49
10	Conclusions	54

1 Introduction

This paper describes a study of the potential contributions of the proposed MATHUSLA detector to the understanding of the origin and nature of cosmic rays by means of extended air showers (EAS). MATHUSLA is designed to search for new physics beyond the standard model, in particular, decays from neutral long-lived particles (LLPs). The detector is to be located on the surface above the CMS (Compact Muon Spectrometer) experiment at the CERN LHC. The proposed MATHUSLA detector has nearly 100% coverage for charged particles over 100 m^2 [1–3]. We show in this paper that by adding a layer of RPC detectors, the MATHUSLA detector can also make important contributions to many unresolved issues in cosmic-ray physics.

In particular, in the next sections, we present the results of a Monte Carlo (MC) study to analyze the sensitivity of MATHUSLA as a detector of cosmic-ray showers. We show that the addition of a layer of RPCs combined with the many layers of scintillating detector planes can provide unique spatial and temporal measurements of EAS. We discuss that such a detector provides information for studies of the energy spectrum, arrival-direction distribution and composition of cosmic rays that can be used for the research on the origin and nature of these particles and for tests of hadronic interaction models. We also discuss the potential for studying inclined events.

Section 2 gives a summary of open questions in the study of cosmic rays and Section 3 a description of the detector as designed to address the particle physics goals. In Section 4 we discuss the addition of a layer of RPC detectors that would allow for detailed measurements of EAS. Section 5 discusses the MC simulations of the production of EAS and the detector response, Section 6 the event reconstruction methodology, and Section 7, the MC event selection. Results of this study are presented in Section 8 and discussed in Section 9. We present our conclusions in Section 10.

2 A glance at cosmic-ray physics

The Earth is being continuously hit by high-energy subatomic particles known as cosmic rays. They are dominated by protons and can have energies as low as some MeV and as high as 10^{20} eV, i.e. orders of magnitude beyond the energies of the most powerful accelerators on Earth [4–6]. Their total energy spectrum can be described by a broken power-law, with a softening at around 4×10^{15} eV (where the spectral index γ changes from -2.7 to -3) and a hardening close to 5×10^{18} eV (at which the spectral index increases to -2.6) [6]. Relative abundances of elemental nuclei in the intensity of cosmic rays are difficult to measure. In spite of this, it has been found that the composition of cosmic rays evolves with the primary energy [6, 7]. In the region below the knee, protons and He nuclei dominates the composition of cosmic rays, while at higher energies the heavier nuclei are more abundant. This happens up to $\sim 10^{17}$ eV, where the composition of cosmic rays becomes lighter. This behavior stops at energies close to the ankle, where an additional transition to the heavy mass group is observed. The evolution of one mass group to another one seems to be correlated with the presence of fine structures in the energy spectrum of cosmic rays [7–11], which, in turn, could be related with acceleration [12] and propagation [13] issues or the transition between different source populations of cosmic rays [11, 14].

The acceleration of cosmic rays may occur in astrophysical plasmas with strong shock waves by means of the so called first-order Fermi acceleration mechanism [15–18], which predicts power-law spectra for the intensity of cosmic rays. The propagation in space of these energetic particles is mainly diffusive due to interactions with the random component of magnetic fields in the interstellar and extragalactic media. As a consequence, the angular distribution of the arrival directions of cosmic rays in the sky seems to be mostly isotropic. There are deviations from isotropy in the sky maps of cosmic rays at the level of 10^{-3} and 10^{-4} , which creates large- and small-scale anisotropic distributions in the sky [19–22]. The large-scale anisotropies are thought to be due to propagation effects and the global distribution of the sources of cosmic rays in the galaxy and in our galactic neighborhood. The details behind the origin of the small-scale anisotropic structures are however less clear. At TeV energies, they may be related with the heliosphere or magnetic turbulences. At tens of EeV, they could be due to some extragalactic sources in the direction of Centaurus and the Ursa Major, as well as the Perseus-Pisces region [23]. A further implication of the diffusive propagation of cosmic rays in the universe is that they loss information about the position of their sources in the sky. Only at extreme energies, the small magnetic deflections of these particles in the space may allow to perform cosmic-ray astronomy [6]. At energies above 10^{18} eV, cosmic rays are of extragalactic origin [24], while below 10^{17} eV, of galactic nature [25]. Somewhere, between 10^{17} and 10^{18} , a transition between galactic and extragalactic cosmic rays is expected [11, 26]. In our galaxy, supernova remnants could be one of the astrophysical sources responsible for cosmic rays of high-energy [24]. However, there are some clues that the galactic center [27] and star forming regions [28, 29] could also accelerate cosmic rays of very high energies in the Milky Way [28]. At ultra high-energies, starburst galaxies are promising candidates [30].

The existence of cosmic rays faces us with several compelling questions about the universe at very high energies. The quest for satisfactory answers to these phenomena is pushed to the limit by

the combined observations of cosmic rays, gamma rays, cosmic neutrinos and gravitational waves [31, 32]. The astroparticle messenger approach calls for scenarios that involve both the domain of elementary particles, the so-called "micro-cosmos", and the realm of the huge celestial objects, what we know as "macro-cosmos".

There are several open questions as to the astroparticle messengers phenomena such as:

- What is the origin of the cosmic-ray particles of extraordinary energy?
- What is the mass composition of cosmic rays?
- What are the phenomena behind the small- and large-scale cosmic-ray anisotropies?
- How are cosmic-rays accelerated to high energies?

When cosmic rays of high energies arrive to the Earth, they collide with the molecules in the atmosphere at altitudes that goes from ~ 15 up to 35 km [33] initiating a set of chain reactions that leads to the production of a cascade of particles that travels at relativistic velocities to the ground. This extensive air shower, as it is known, contains a large number of particles, which depends on the primary energy of the cosmic ray and increases according to a power-law function. The air shower has electromagnetic, penetrating and hadronic components. The first one is most abundant and is composed of photons and e^\pm 's, the second one, by μ^\pm 's, and the last one, by nucleons, mesons, and atomic nuclei. During their development in the air, EAS produce radio and Cherenkov radiation [4]. Also, the atmosphere emits fluorescence light from the excitation of nitrogen molecules [6].

At energies above 10^{13} eV, cosmic rays are detected indirectly from the measurements of EAS using arrays of particle detectors, radio antennas, Cherenkov and fluorescence telescopes that are displayed over large surfaces [4]. At energies smaller than 10^{15} eV, cosmic-ray studies are observed in a direct manner from balloon-borne and satellite instruments [6, 34].

Data collected by many ground and underground-based observatories as well as by sensitive radiation detectors installed on balloons and also on satellites orbiting Earth [35–41] have provided much information on the energy spectrum, arrival direction and mass composition of cosmic rays that have revealed very important clues about the nature, propagation, acceleration mechanism and the origin of these energetic particles [24, 42–47]. In addition, observations from the northern hemisphere of high-energy gamma rays reveals many potential sources of cosmic rays within our galaxy [27, 48–50].

Notwithstanding these excellent measurements, the abovementioned questions still remain without conclusive answers. They will be addressed by a new generation of ground-based observatories, some of which are located at high altitudes (~ 4500 m a.s.l) in the Earth's southern [51, 52] and northern hemispheres [53], and by new space-based instruments [54]. In addition, multiwavelength and multimessenger observations will play an important role in these tasks [31, 32]. We demonstrate in this paper that the MATHUSLA detector could also make important contributions to advancing the understanding of the astrophysics and physics of high-energy cosmic rays.

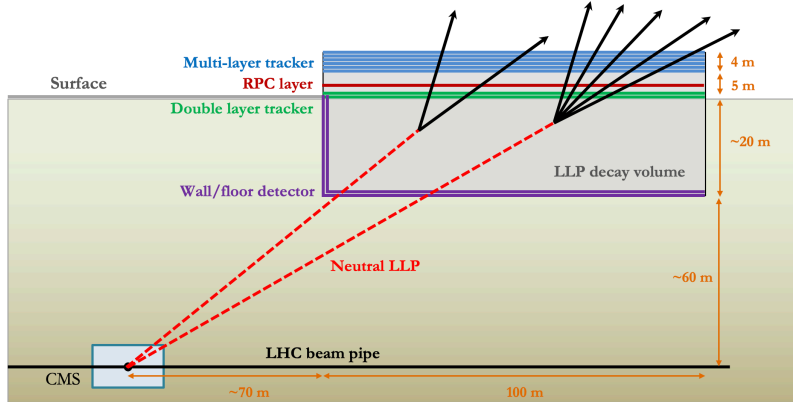


Figure 1. MATHUSLA detector at CMS site [3].

3 The MATHUSLA Detector

The proposed MATHUSLA detector shown in Figure 1 will be located on the surface above the CMS [55] pp interaction point (IP) located on CERN-owned land. The proposed goal is to have MATHUSLA ready to take data when the High-Luminosity LHC (HL-LHC) [56] turns on.

To have sufficient solid-angle coverage, the current detector concept, shown in Fig. 2, is a $100 \times 100 \text{ m}^2$ detector consisting of a hundred $9 \text{ m} \times 9 \text{ m}$ units. Each detector unit comprises 9-layers of scintillating-detector planes that provide position and timing coordinates of charged particles resulting from the decay of long-lived particles in the MATHUSLA detector decay volume. There are five detector planes at the top, two additional planes 5 m below (to enhance the particle position measurement precision close to the floor), and two additional planes at the floor (to veto charged particles from the LHC and cosmic-muon backscattering). The total height of $\sim 40 \text{ m}$ includes a $\sim 25 \text{ m}$ LLP decay volume, 21 m of which is below ground, and 17 m above ground that houses the tracker and the crane system used for assembly and maintenance.

The layout of the building that houses the $100 \text{ m} \times 100 \text{ m}$ experimental area and the $30 \text{ m} \times 100 \text{ m}$ adjacent area for the detector assembly is shown in Figure 3. The structure, which is located on the surface near the CMS IP fits well on CERN-owned land. Having a large part of the decay volume underground brings it closer to the IP, which increases the solid angle in the acceptance of LLPs generated in the collisions. To adjust to the available land, this proposal has a 7.5 m offset to the centre of the beams. The site allows for the detector to be as close as 68 m from the IP, which is shown in red in Figure 3

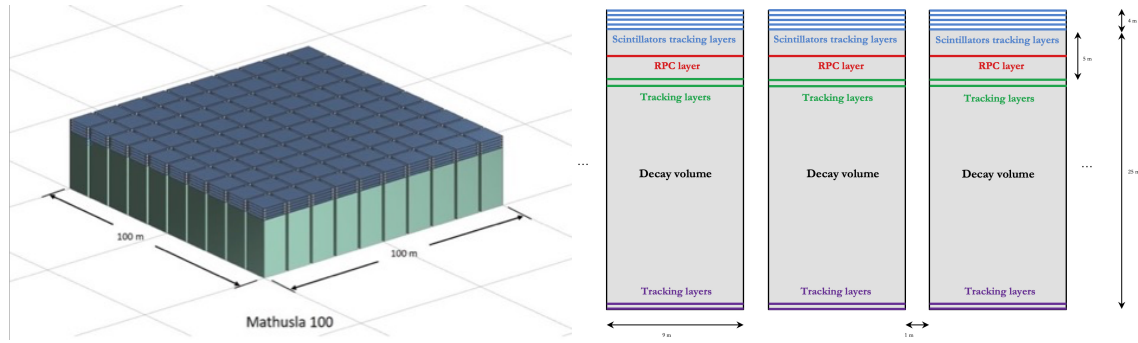


Figure 2. Schematic view of the MATHUSLA detector modular concept [3].

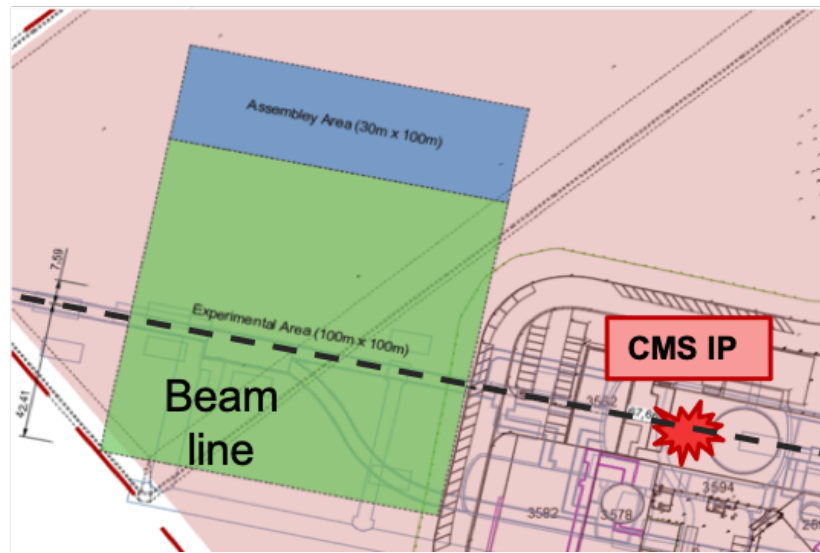


Figure 3. MATHUSLA detector at CMS site [3].

3.1 Scintillating Detector Planes

Each of the $9\text{ m} \times 9\text{ m}$ detector planes consists of an assembly of extruded scintillating bars whose length, width and thickness are typically 4.6 m , 4.5 cm , 2 cm , respectively. Each bar is extruded with a hole at the centre into which a wave-length shifting (WLS) fibre is inserted and connected at each end to a SiPM. The coordinate along the length of the bar is determined by differential time measurement at the two ends of the bar with resolution $\sigma \sim \pm 15\text{ cm}$. The width of the bar determines the corresponding transverse coordinate with $\sigma = \pm 1.3\text{ cm}$. Figure 4 shows some typical extruded scintillating bars produced at the Fermi National Accelerator Laboratory (FNAL).

To facilitate installation the scintillating bars are assembled into 4 sub-units that comprise ~ 100 bars resulting in $\sim 4.5\text{ m} \times 4.5\text{ m}$ sub-units that allow for overlapping the 4 sub-units longitudinally and transversely to avoid gaps in coverage. In this arrangement the 4 sub-units provide hermetic



Figure 4. Extruded scintillating bars produced at FNAL with one and two holes for WLS fiber insertion.

surface-coverage over a $\sim 9 \text{ m} \times 9 \text{ m}$.

3.2 Cosmic Rays

The dominant background to long-lived particle searches in the MATHUSLA detector is cosmic rays. Timing information from the scintillating bars allows for the rejection of downward-going charged cosmic rays. The two-floor detectors provide rejection of inelastic back-scattering of cosmic-ray muons striking the surface and muon decays that send an upward electron through the detector planes. They also serve to reject inelastic interactions of muons near the surface. Several simulation studies show that these backgrounds can be rejected. A more detailed description of the possible backgrounds can be found in [2].

MATHUSLA, equipped with seven scintillating detector planes at the top of the instrument that has good space and time resolution (see section 3.1) and nearly continuous coverage over an area of 10^4 m^2 , is also sensitive to air showers induced by cosmic rays. However, it is limited as an air shower detector because the long scintillating bars are not able to provide coordinates of several charged tracks hitting the same bar at nearly the same time. Such occurrences lead to saturation and loss of information.

4 The RPC detector

4.1 Introduction

The peculiarity of MATHUSLA, as a cosmic-ray experiment, is that its detector is primarily conceived for searching for very long-lived particles produced by pp interactions in the LHC. Studying its performance as a cosmic-ray detector, and substantially improving it with a special sub-detector dedicated to the study of extensive cosmic-ray showers, is discussed in this section.

The main constraints imposed by the primary purpose of the experiment are the operation at CERN’s very modest altitude (373.6 m.a.s.l.) and the sensitive area not exceeding 10^4 m^2 . On the other hand, MATHUSLA, equipped with 10 scintillating planes that provide good spatial resolution and one ns time resolution is an unprecedented large area cosmic-ray tracker.

Taking into account the features described above the cosmic-ray search of MATHUSLA may be focused on the following main items:

- Cosmic-ray composition, i.e. measurement of the atomic number Z of the primary particle.
- Parallel-muon bundles crossing the detector. In this case, a “pure muonic shower” is observed. For inclined or almost horizontal showers that traverse a larger thickness of the atmosphere where the hadronic component is absorbed, purer muonic showers can be observed at high and very high energies.

However, a scintillating tracker such as MATHUSLA has the following limits for detecting EAS:

- Limited resolution for multiple-track detection. The limit is no more than approximately 1 track in a scintillating bar of area $(450 \times 4.5) \text{ cm}^2 = 2025 \text{ cm}^2$. Multiple tracks in the same scintillating bar, in addition to being counted as a single track, also spoil the timing information and do not allow localization of the track position along the scintillating bar. This severely limits the study of parallel-muon bundles, which is an excellent field of investigation where MATHUSLA could be competitive with other cosmic-ray experiments.

The MATHUSLA scintillating bars do not provide energy deposition measurements that are extremely important for the shower-core detection where the hits produced by electro-photonic component can reach a density of 10^6 m^{-2} for a primary cosmic-ray particle of 1 PeV.

- Absence of an obvious muon-identification strategy, which is normally based on a heavy-material layer absorbing secondary particles except muons. This is impossible for MATHUSLA and requires a different strategy. It should be stressed that muon detection is important in any channel of cosmic-ray search, but it is crucial in particular for gamma-hadron discrimination. A possible muon-detection alternative strategy could be based on the identification of the regular linear pattern of a muon track from the random hits produced by the electro-photonic component of the shower. This could be possible thanks to the tracking capability of MATHUSLA. The expected efficiency of this method in identifying a muon would be modest. However, at about 1 PeV a proton shower produces an order of 10^4 muons, and the identification of just one of them would be sufficient to reject the shower as a gamma ray candidate.

4.2 The RPC sub-detector

The addition of a single RPC layer to the layers of MATHUSLA scintillating detectors can significantly enhance the capability of the instrument to make detailed measurements of EAS. In this section, we describe the RPC chambers, the proposed layout for MATHUSLA, and the front-end electronics. The proposed RPC configuration profits from the experience obtained during 5 years of operation of the ARGO-YBJ experiment [57]. The main difference compared to ARGO-YBJ is that the RPC

chambers for MATHUSLA will operate in avalanche mode instead of the streamer mode chosen for ARGO-YBJ. Operating in avalanche mode requires improved front-end electronics to compensate for the smaller charge and lower discrimination threshold, which has the advantage of substantially extending the linear response range of the analogue readout [58].

The gas-gap thickness is another difference with respect to ARGO-YBJ. At the ARGO-YBJ altitude of 4300 m a.s.l., the atmospheric pressure was about 600 mbar to be compared with the CERN pressure of 980 mbar. This makes possible a substantial reduction of the gap with respect to the 2-mm gap of the ARGO-YBJ RPCs. We are testing 1-mm gas gaps that will be used for the BI RPCs of the ATLAS muon spectrometer [59]. The choice of the 1-mm standard for the gap size of the MATHUSLA RPCs allows us to exploit the research and development of the ATLAS Phase II upgrade. A further advantage of reducing the gap size to 1 mm is improved time resolution. The MATHUSLA RPC gas gap is schematically shown in Fig. 5

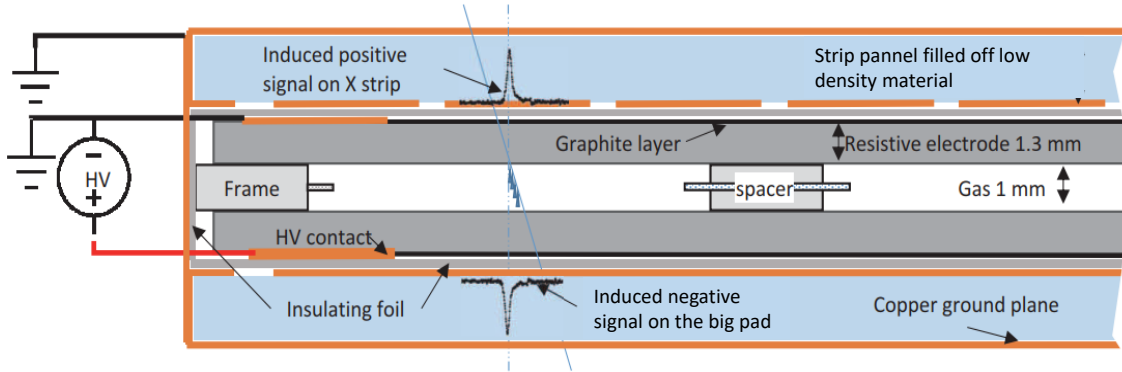


Figure 5. RPC gas gap sandwiched between the strip and the “big pad” panels. The main components are the high-pressure laminate electrode plates, the graphite electrodes, the insulating PET foil, and the spacers.

The main RPC parameters that can be easily optimized concern the read-out granularity. Following the ARGO-YBJ scheme there are two types of read-out electrodes: the digitally readout strips located on top of the gas gap in Fig. 5 and the “big pads”, located below the gas gap in Fig. 5. The pads are large area capacitors, covering half of the gap area, and integrate the charge of all hits located in the corresponding pad area. The analog readout of the pad signal makes it possible to measure the shower-core multiplicity when it is so high that the digital readout is saturated. The strips, longitudinally oriented, are 2.2 m long with an 11.2-mm pitch with front-end electronics located at both ends in order to determine the hit position along the strip using the signal arrival time at the two ends. The area of the strips, 242 cm^2 , is substantially smaller than the area of the scintillating bars, 2025 cm^2 , which significantly reduces the probability of multiple hits in the same strip. This is particularly important for the detection of parallel muon bundles where the probability of two or more muons striking the same scintillating bar is large as well as for selecting straight tracks from the background of randomly distributed hits due to the electro-photonic component of the shower.

The 0.99 m^2 “big pads” ($1.1 \times 0.9 \text{ m}^2$), are smaller than those of ARGO-YBJ (1.75 m^2) and

provide better detail of the shower-core profile. This is important for identifying showers generated by different kinds of primary cosmic rays. For example, gamma showers have a very compact single core compared to the less compact multiple-core structure of hadron showers. Moreover, the high-Z primary showers are broader than proton showers and have a substantially larger multiplicity of different cores.

These qualitative considerations need to be studied in detail with an adequate simulation in order to optimize the granularity of both strips and “big pads”, both of which can be easily tuned for specific physics channels.

The RPC characteristics are the following:

- Gas gap: a single 1-mm gap of area $(2.2 \times 0.9) \text{ m}^2$ with 2 gas inlets and 2 outlets at the corners.
- Strip read-out panels: 80 longitudinal strips 2.2 m long with 11.2-mm pitch. Front-end boards are located at both ends of the strip for interpolating the position along the strip. The alternative solution with the strips oriented along the short side of the chamber can also be considered but it is less practical for the final assembly of the chamber.
- “Big pads” for the analogue read-out of area $(1.1 \times 0.9) \text{ m}^2$
- Front-end electronics embedded in the same Faraday cage of the detector
- Mechanical support structure made with honeycomb panels about 1 cm thick.

In order to fulfill the requirements of the $9 \times 9 \text{ m}^2$ super-modulus, 4 chambers are assembled in the same mechanical structure of $9 \times 0.9 \text{ m}^2$ size, as shown in Fig. 6. The gas is serially distributed from one gap to the next. The structure supporting the 4 chambers is made of two “C”-shaped aluminum profiles fixed at the sides of the chambers (as shown in Fig. 7). This structure behaves as a stiff beam supported only at the ends, with a sagitta of about 1-cm. The thickness and the height of the profiles need to be optimized taking into account the weight of the structure. In the final assembly of a $9 \times 9 \text{ m}^2$ super-modulus, two “C”-shaped profiles in contact with one another are screwed together in a single “I”-shaped profile.

4.3 The RPC front-end electronics

The front-end circuit was developed at the INFN laboratory of Rome Tor Vergata for the RPC detectors of the ATLAS LHC phase-II upgrade [59]. The circuit consists of a charge preamplifier, a discriminator, and a Low Voltage Differential Signal (LVDS) driver, shown schematically in Fig. 8. The amplifier and the driver are built as discrete component circuits. The discriminator is a full-custom circuit, conceived with the purpose of optimizing performance and allowing for large mass production at low cost

4.3.1 Preamplifier

The preamplifier uses Silicon Bipolar Junction Transistor (BJT) technology. The main feature of this new kind of preamplifier is fast charge integration with the possibility of matching the input

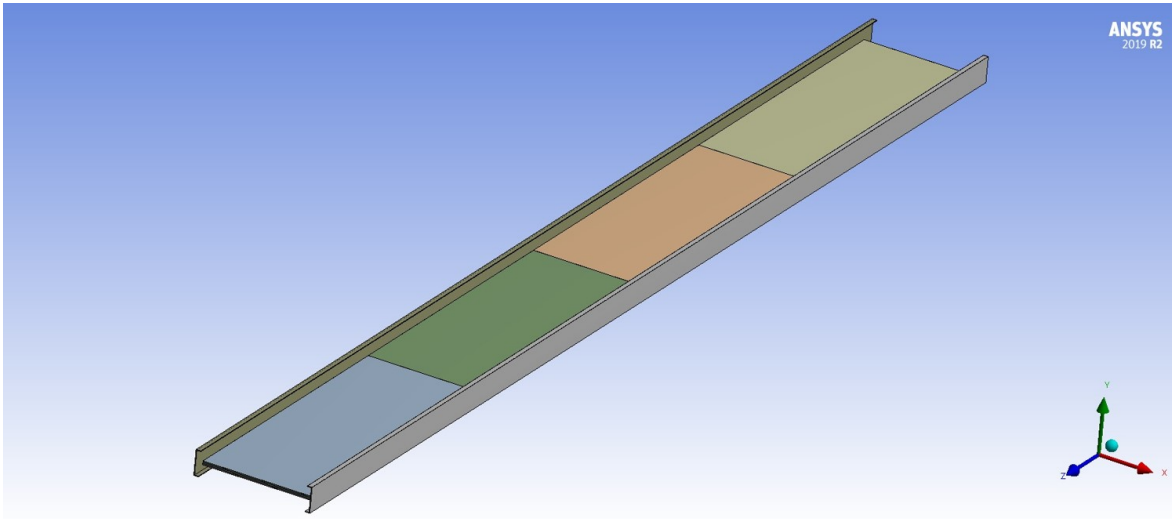


Figure 6. Schematic of one RPC unit with four chambers assembled in a line within the same mechanical structure.

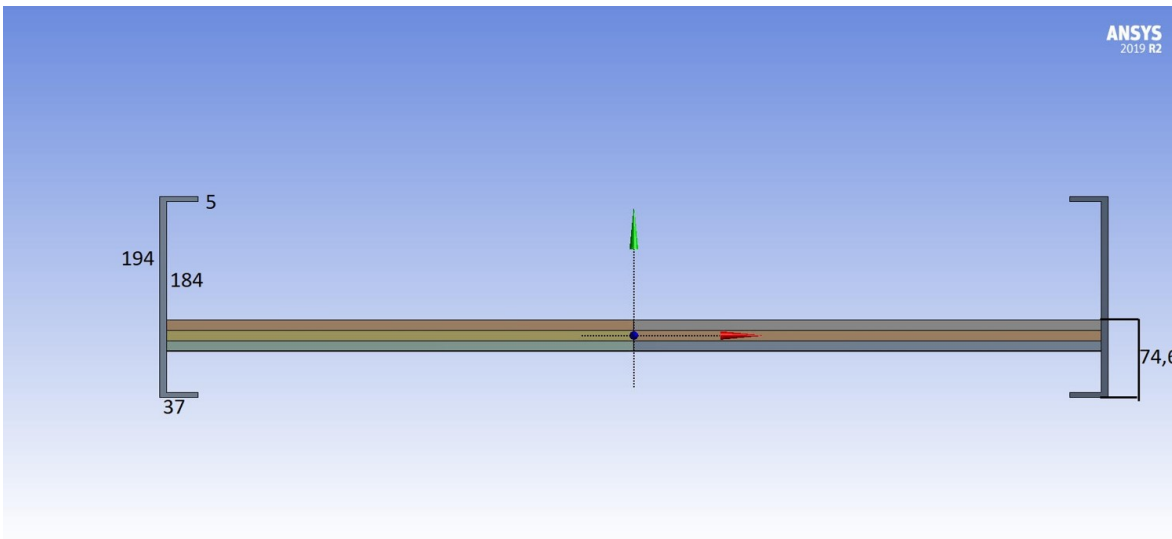


Figure 7. Schematic side view of one RPC unit showing details of its mechanical structure with the two “C”-shaped profiles. All the values displayed in the figure are in mm.

impedance to a transmission line. Its working principle is shown in Fig. 9, which explains how the injected signal is integrated.

The specifications of the Silicon BJT technology planned for the charge preamplifier are listed in Table 1.

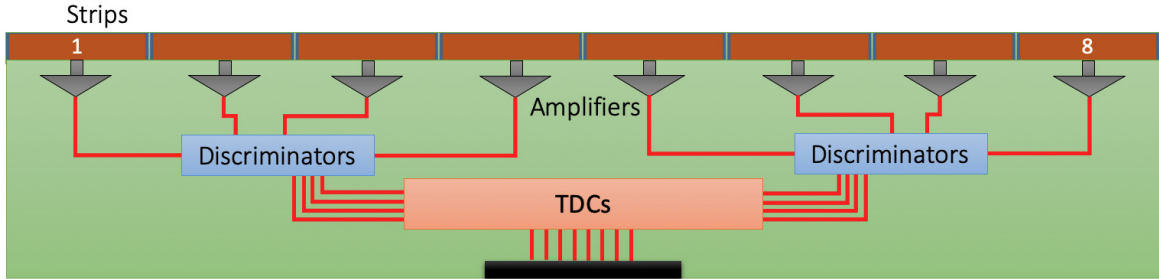


Figure 8. Logical layout of an 8-channel RPC front-end circuit board.

Table 1. Specifications for the preamplifier in the RPC front-end circuit.

Voltage supply	3 – 5 V
Sensitivity	0.2 – 0.4 mV/fC
Noise (independent of the detector)	1000 e ⁻ RMS
Input impedance	50 – 100 Ω
Bandwidth	10 – 100 MHz
Power consumption	5 mW/ch
Rise time for $\delta(t)$ input	300 – 600 ps

4.3.2 Discriminator

The requirements for the MATHUSLA cosmic-ray RPC discriminator are the following: a) very low threshold, of the order of 6-7 mV, and b) efficient operation with very fast pulses like the ones produced by RPCs. The very low threshold for cosmic shower detection is not required to improve the rate capability, which is very modest in this case, but rather to improve the linearity range in the measurement of the hit density inside the shower core. The core of the showers can have hit densities exceeding $10^6/\text{m}^2$, due to the very high energy of the primaries. In this case, the linearity range requires that the charge released in the gas by a single hit is very modest. The above requirements are met with a new type of discriminator based on the saturated amplifier: a signal above the discrimination threshold is amplified by multiple stages up to saturation. The output is a square wave of fixed amplitude independent of the input signal. Its duration is the time over the threshold of the input signal, which allows measuring the input amplitude, once the input shape is known. This type of measurement uses a logarithmic scale. This is a crucial characteristic when the input charge can vary over a wide range. In the case of MATHUSLA, the number of particles in a single front-end channel may range over several orders of magnitude, depending on the shower energy and the read-out strip area.

The discriminator circuit is schematically shown in Fig. 10 (a). The first stage is a simple amplifier in the BJT common-emitter configuration. The following three stages can be represented as logic “NOT” gates and have the task of discriminating (first logic stage) and saturating the input signal. As shown in Fig. 10 (b), for each logic stage the output shows sharper edges and the final

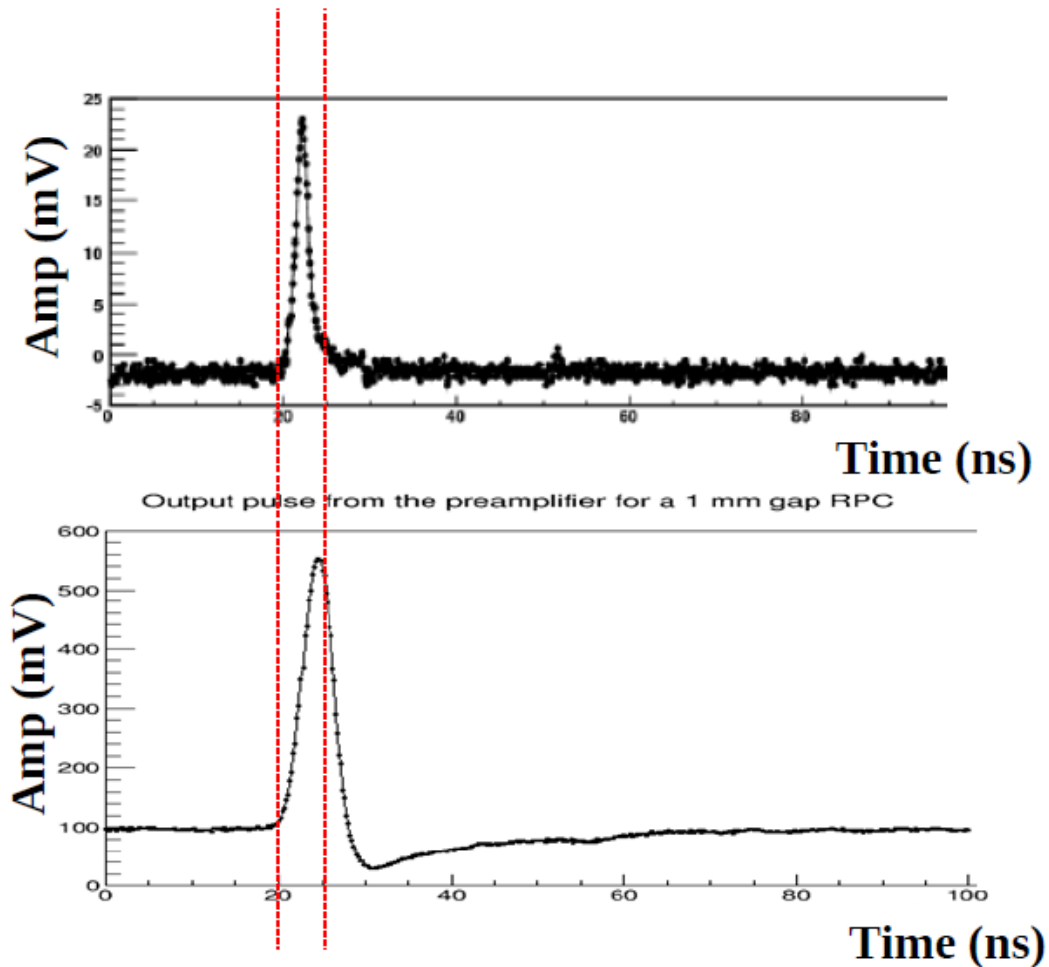


Figure 9. Comparison between a bare RPC signal (upper plot) and the corresponding amplified signal (lower plot).

output is a rectangular wave of inverse polarity with respect to the analogue input. The discriminator features are summarised in Table 2.

4.3.3 TDC

In a system with a very large number of channels, where time measurements are required, time digitization is one of the most relevant problems due to cabling complexity and TDC cost. For the system proposed for MATHUSLA cosmic-ray measurements, the TDC is embedded in the front-end electronics and is included in the full-custom circuit under development. This is possible thanks to new technologies, 120-nm SiGe and CMOS, which make possible oscillators and counting scalars that operate at 2 – 3 GHz. For the detection of a large-size cosmic shower, the intrinsic single-hit time

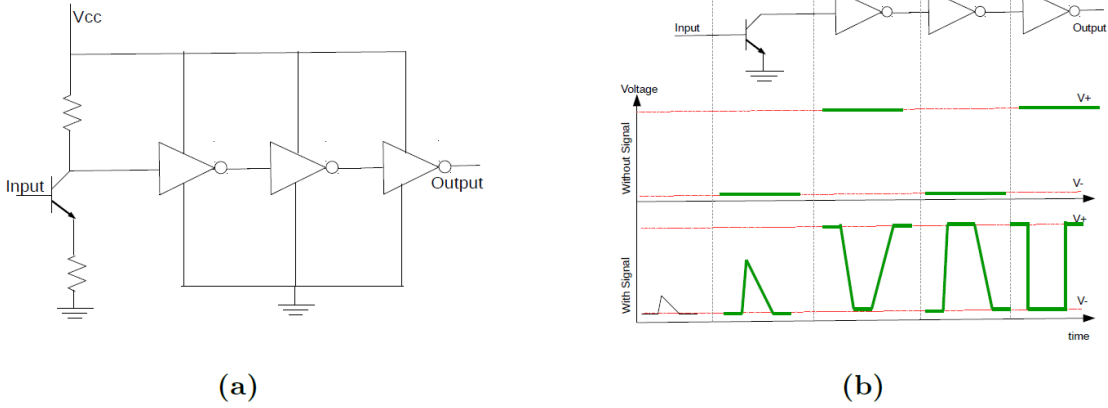


Figure 10. (a) Schematic of the discriminator circuit. (b) Signal-processing scheme for the discriminator circuit.

Table 2. Specifications for the discriminator in the RPC front-end circuit.

Technology	130 nm Si-Ge BiCMOS
Voltage supply	1 – 2.5 V
Minimum threshold	0.3 μ V
Minimum input-pulse width for threshold linearity	0.5 ns
Bandwidth	10 – 100 MHz
Power consumption	10 mW/ch
Rise time for $\delta(t)$ input	300 ps
Input impedance	100 Ω
Double-pulse separation	1 ns

fluctuations are in the nanosecond range, and therefore a TDC of comparable accuracy would be suitable for this purpose. This makes possible a drastic simplification for the TDC. Indeed, at a frequency of 2 – 3 GHz, the simple counting of the periods covering the time interval under measurement results in an uncertainty of 0.5 – 0.3 ns that is adequate for cosmic-shower timing, and no interpolation between two consecutive clock signals is required.

4.3.4 Trigger and data acquisition

This section describes the MATHUSLA cosmic-ray trigger and its implementation in the electronic circuits that produce the trigger signal and give the Data Acquisition the start signal. The trigger logic

presented here is fully based on the signals supplied by the RPC-layer detector, consequently, the cosmic ray trigger is independent of the main long-lived particle trigger of the experiment.

The MATHUSLA trigger of an EAS generated in the atmosphere by a cosmic primary particle is based on the multiplicity of the shower hits detected by the RPC layer. This multiplicity is approximately proportional to the EAS shower energy on a logarithmic scale. Thus, a multiplicity threshold is equivalent to an energy threshold, even within the large fluctuations of the energy vs. multiplicity correlation. The main task of a multiplicity trigger is to select the simultaneous hits due to an EAS from the accidental rate due to the combinatorial background of the counting rate over a large-area detector. Simultaneous hits due to a cosmic shower can be selected by a proper coincidence among several chambers. The main challenge of this trigger is that the time resolution of the coincidence must take into account the systematic delay among different hits due to the inclination of the shower front with respect to the vertical direction. For showers propagating almost horizontally this delay is of the order of the linear detector dimension over the speed of light, L/c . For a $(100 \times 100) \text{ m}^2$ detector like MATHUSLA, this delay can be as large as $(100\sqrt{2} \text{ m})/c$, namely about 450 ns, assuming the diagonal as the maximum distance between two hits. This large delay does not allow for a coincidence time, which is the main parameter for reducing the accidental rate. This problem can be solved by dividing the detector into subdetectors of gradually increasing areas where the coincidence time resolution can be improved according to the smaller subdetector size. In this section, we give an example of how this trigger concept can be implemented inside the MATHUSLA cosmic-ray detector and how the accidental rate can be evaluated. A more precise trigger study, including the efficiency vs. energy correlation as well as the trigger counting rate, for each multiplicity threshold, requires a full simulation of the process starting from the characteristics of the shower to be triggered.

Table 3. Specifications for the relevant RPC trigger parameters.

Effective detection area for each submodule	$(9 \times 9) \text{ m}^2$
Assumed counting rate per unit area	1 kHz/m ²
Multiplicity threshold for EAS detection	50 hits
Number of RPC sub-modules	100
Number of chambers in one RPC sub-module	40
Trigger majority threshold in one sub-module	2 hits
Time resolution for a submodule majority	50 ns
Maximum time delay for inclined showers in one sub-module	42 ns
RPC read-out strip length	2.2 m
Inverse signal propagation speed	5 ns/m

In order to evaluate the efficiency of rejecting the accidental background rate and to support it with some numerical calculations we assume the following working conditions:

- Multiplicity threshold of 50 hits on the whole RPC detector. The corresponding energy threshold should be at least an order of magnitude higher than that of ARGO-YBJ if renormalized to the much lower altitude of MATHUSLA.

- Intrinsic detector counting rate equal to 1 kHz/m². This is an overestimation of the expected rate, in order to obtain a very conservative evaluation of the accidental background rate.
- The hits due to the shower are randomly distributed over the detector. This is also a conservative hypothesis for the accidental background calculation because the shower hits tend to be clustered thus giving a higher probability of several hits in the same sub-detector, which is a crucial point in the following trigger project.

The relevant parameters for the MATHUSLA RPC trigger are listed in Table 3 and will be used in the calculations reported below. The smallest subdetector where the shower multiplicity is considered for trigger purposes is an RPC sub-module of about (9×9) m². The MATHUSLA detector, according to Fig. 2, is subdivided into 100 such units. Each unit contains an RPC plane of the same area, consisting of 40 chambers arranged in groups of 4 chambers in the same mechanical support as shown in Fig. 6. The first step of the proposed trigger requires selecting all submodules with at least 2 hits due to the shower. For each sub-module, the analog sum of all output signals from the front-end circuits is sent to a discriminator with a threshold requiring at least two simultaneous signals. The signal shaping time is 25 ns, resulting in a time resolution of about 50 ns of this majority coincidence. This covers the uncertainties due to both the shower inclination, 42 ns for a (9×9) m² sub-detector, and the timing propagation of the signal along the readout strips (namely $2.2 \text{ m} \times 5 \text{ ns/m} = 11 \text{ ns}$) combined in quadrature. The sub-module counting rate is 81 kHz so that the accidental coincidence rate is $(81 \times 10^3 \text{ Hz})^2 \times (50 \times 10^{-9} \text{ s}) = 328 \text{ Hz}$ for each of the 100 submodules comprising the RPC detector.

The probability of missing the trigger, because all shower hits fall in different sub-detectors, is extremely small. For a 50 hits shower, the average number of hits/subdetectors is 0.5 and the expected number of towers showing a coincidence of at least 2 hits is 9.02, according to Poisson statistics.

The next step in the trigger logic is to require the coincidence with a proper multiplicity on the whole detector. Repeating the procedure followed for the single units, the analog sum of the 100 tower outputs is sent to a discriminator with a selectable threshold requiring the coincidence of two or more towers on the whole detector. The total rate of the analog sum is $328 \text{ Hz} \times 100 = 32.8 \text{ kHz}$. The coincidence time, in this case, must be 450 ns to take into consideration the maximum time uncertainty due to the shower inclination over the whole detector. For a multiplicity threshold of 2 subdetectors out of a hundred, the accidental rate is: $(32.8 \times 10^3 \text{ Hz})^2 \times (450 \times 10^{-9} \text{ s}) = 427 \text{ Hz}$ which is a modest trigger rate.

The probability of missing the trigger for a shower of 50 hits is negligible. Indeed, the probability of less than two sub-detectors firing for an expected number of 9.02 is 1.23×10^{-3} . If needed, the trigger rate can further be decreased by increasing the multiplicity threshold above 2. For a threshold of 3, the accidental rate is $(32.8 \times 10^3 \text{ Hz})^3 \times (450 \times 10^{-9} \text{ s})^2 = 7.1 \text{ Hz}$.

4.3.5 Time schedule

The front-end circuit described here is not yet fully developed. The preamplifier and the discriminator are operational and are included in the RPCs currently being installed for the ATLAS Phase-I upgrade.

The integration of the TDC in the circuit is in progress. It requires 1-2 further foundry runs in the next 1-2 years. The current plan is to be ready for the LHC Phase-II upgrade.

5 Simulations

In order to explore the performance of the RPC layer and the scintillating planes of MATHUSLA as air-shower cosmic-ray detectors, we have prepared a set of toy MC simulations that include the production of EAS by the primary cosmic rays, the evolution of the particle cascade until its arrival at the Earth’s surface and the physical response of the detectors to the passage of the shower particles. In the following subsections, we describe each of the above simulation steps that are used to produce our MC data.

5.1 Air shower simulations

For the generation and development of EAS in the atmosphere, we followed the procedure described in [2]. In particular, we employed the CORSIKA v7.71 package without thinning [60] together with the FLUKA 2020 [61, 62] and the QGSJET-II-04 [63, 64] hadronic interaction models. FLUKA was used to simulate collisions with hadron energies $E_h < 200$ GeV, while QGSJET-II-04 was employed to describe hadronic interactions with higher energies. CORSIKA simulates the evolution of the particle cascade through the atmosphere from the production point to the detector level. The output provides information about the spatial, time, and momentum distributions of the shower particles at the observation point. Without thinning, CORSIKA follows the history of each particle in the EAS until its energy falls below a certain threshold, which is specified at the beginning of the simulation chain. Here, we kept the CORSIKA default values of 3 MeV for shower electrons and gamma-rays, and 100 MeV for shower muons and hadrons.

We chose the U.S. standard atmosphere model in our simulations. In addition, we selected the curved atmosphere option, as we will work also with very inclined showers. Moreover, the observation level was set at 436 m a.s.l. ($X \sim 1000$ g/cm²) and the local geomagnetic field was chosen as $B_x = 22.2 \mu T$ and $B_z = 41.9 \mu T$ in the simulations. Such values¹ correspond to the characteristics of the site above the ATLAS interaction point, which was initially considered as one of the potential places of the MATHUSLA experiment. The differences with the location of MATHUSLA at the CMS site are small (the altitude is about 374 m a.s.l. and the corresponding magnitudes of the geomagnetic field are $B_x = 22.2 \mu T$, $B_z = 42.1 \mu T$). Therefore, our conclusions regarding the performance of the MATHUSLA detector are not expected to be affected by such differences.

The EAS were produced with a $\sin \theta \cos \theta$ distribution for two zenith angle intervals: $\theta = 0^\circ - 20^\circ$ (vertical EAS) and $\theta = 70^\circ - 80^\circ$ (inclined EAS), and the shower cores were scattered randomly on the MATHUSLA area. A flat geometry was employed. We produced MC simulations for H and Fe primary nuclei with energies between 1 TeV and 1000 PeV assuming an energy spectrum of the form E^{-2} . In order to improve the statistics at the highest energies, we generated MC simulations

¹The data was taken from the NOAA (National Centers for Environmental Information) webpage at <https://www.ngdc.noaa.gov/geomag-web/>.

by energy decade as shown in Table 4. Each event was weighted to achieve a unique E^{-2} energy spectrum for the whole energy range.

Table 4. Distribution of the total number of CORSIKA simulations generated by energy decade. CORSIKA version 7.71 was used together with the FLUKA and QGSJET-II-04 hadronic interaction models.

Energy decade	v7.71	
	$0^\circ - 20^\circ$	$70^\circ - 80^\circ$
1-10 TeV	2×10^4 H	2×10^4 H
	2×10^4 Fe	2×10^4 Fe
10-100 TeV	2×10^4 H	2×10^4 H
	2×10^4 Fe	2×10^4 Fe
100-1000 TeV	1×10^4 H	1×10^4 H
	1×10^4 Fe	1×10^4 Fe
1-10 PeV	7.5×10^2 H	1×10^3 H
	7.5×10^2 Fe	1×10^3 Fe
10-100 PeV	1×10^2 H	2.5×10^2 H
	1×10^2 Fe	2.5×10^2 Fe
100-1000 PeV	3×10^1 H	2.1×10^2 H
	2×10^1 Fe	1.5×10^2 Fe

5.2 Simulation of the MATHUSLA detector

For our study, we built a toy MC model of MATHUSLA using a program written in ROOT CERN [65]. In particular, we considered a simple geometry consisting of seven extruded scintillating detector layers and the RPC layer as shown in Fig. 1. The present work did not incorporate the last design of MATHUSLA, but a previous one. However, we do not foresee substantial modifications to the main results on the performance of the experiment for cosmic-ray detection. In our simulations, the two scintillating detector layers near the bottom of the instrument are ignored. On the other hand, the RPC chamber plane is located 2 m above the intermediate scintillating detector layer that is found in the middle between the top and intermediate groups of scintillating detector planes. Hence, we have five detector layers above the RPC and two of them below it (see Fig. 2). The size of the detector was set to $100 \text{ m} \times 100 \text{ m}$. The coordinate system is oriented so that the X and Y axis are parallel to the horizontal dimensions of the detector. In this coordinate frame the detector plane extends from $x, y = 0 \text{ m}$ to 100 m , and from $z = 0 \text{ m}$ to 9 m . The height is measured from the bottom of the intermediate tracking detector layer.

The RPC geometry used assumes Big Pads with a conservative size of $1 \text{ m} \times 1 \text{ m}$. These elements provide not only spatial and time data of the shower particles but also local particle density measurements. We output the coordinates of the central positions of the Big Pads that were hit, the arrival times of the first shower particles in each module, and the induced signals. Space-time measurements of the EAS can be made with individual RPC strips, but to keep the simulation as simple as possible, we have focused our studies on the data from the Big Pads. The amplitudes of the RPC-pad signals

are assumed to be proportional to the density of charged particles as found by the ARGO-YBJ RPC measurements [66]. We must point out that in a real simulation, it must be considered that the Big Pads can only be used to measure hit multiplicities with high densities due to their high capacitance. For small density measurements and individual hit counting, the RPC strips will be used.

For the simulations, the scintillating bars have a length of 5 m and a width of 4 cm. They are oriented along the same direction on each plane (parallel to one of the X or Y axis), but they are rotated by 90° when passing from one scintillating plane to another one. In the MC simulations, we have considered that the scintillating detector layers are sensitive only to the passage of charged particles and that the output saturates for more than one hit. Our assumption is conservative. In practice, the scintillating detector bars will saturate on average at one hit per bar. Consequently, the simulation assumes that the scintillating bars provide information of the impact point and arrival time only for hits of single-charged particles. In case of more than one hit per bar, we only save the central coordinates of the corresponding bar. For more reliable estimations of the performance of the scintillating detector layers, detailed simulations are needed. This task will be done in a future study. Finally, in our simulations, we have considered that the RPC and the scintillating detector planes have a 100 % efficiency for the detection of charged particles.

To initiate the simulation, the cores of the CORSIKA air showers were randomly distributed in the instrumented area of the detector. Then we injected the shower particles that reach the detector level at the top layer of MATHUSLA. We followed their trajectories through the tracking planes and recorded the spatial coordinates of the hit modules and the corresponding hit times, the latter only in case of one hit per bar. For the Big Pads of the RPC, we also saved the output signals, which are proportional to the local number of incident particles. For the simulations of the detector performance, we only used e^\pm 's, μ^\pm 's, p^\pm 's, charged pions and kaons. We allowed unstable particles to decay and removed their decay products from the simulations. The lifetimes of the decaying particles were taken from [7]. In addition, we neglected the energy losses of the EAS particles due to interactions with the detector and the air between the tracking layers. We assumed that the entire surface of the detector layers of MATHUSLA are active areas, with no gaps between contiguous scintillating bars or Big Pads.

To illustrate the output of the simulation, in Figs. 11 and 12, we present two examples: one for a vertical shower and another one for an inclined EAS, respectively. In these figures, we display the 3D patterns of hits at the MATHUSLA detector, the corresponding generated signals at the RPC layer, and the arrival times of the 1st particles hitting each Big Pad of the RPC.

6 Event reconstruction

6.1 Shower core position

The reconstruction procedure of the EAS events in our analysis goes through different phases. In the first stage, the shower core position and the arrival direction of the EAS are estimated. To find the core position a simple algorithm is applied. For each tracking plane, as a first approximation to the shower core positions, we used the barycenter of the respective signal distributions in the XY space,

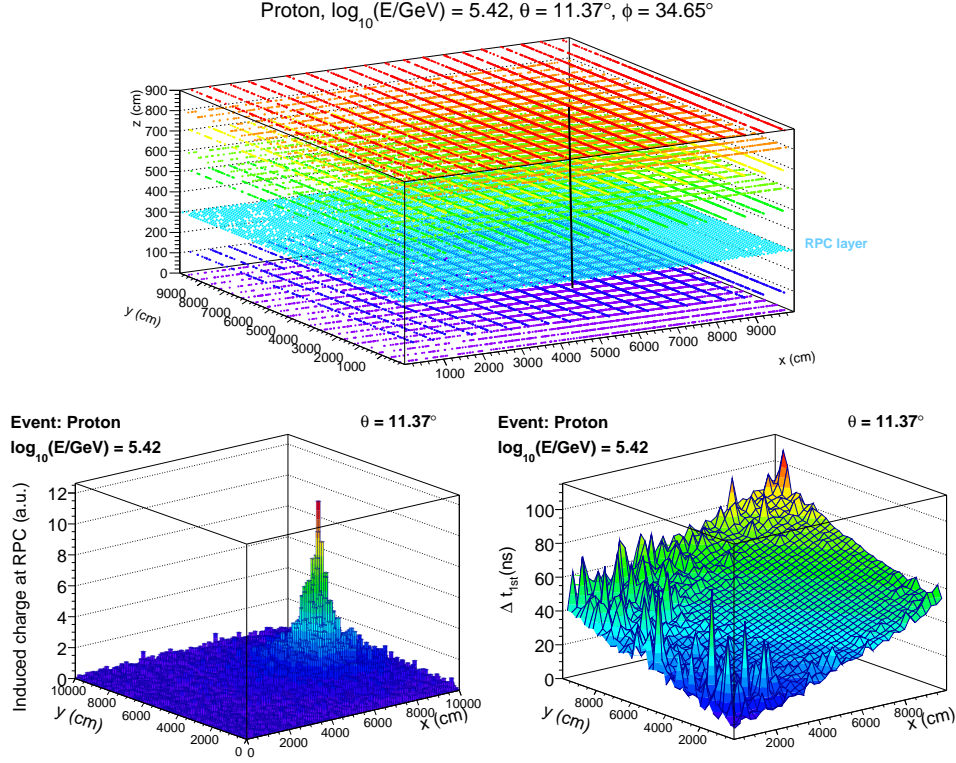


Figure 11. Example of a simulated vertical EAS impinging on the MATHUSLA detector. The event was induced by a primary proton with an energy of $\log_{10}(E/\text{GeV}) = 5.42$ and arrival direction $(\theta, \phi) = (11.37^\circ, 34.65^\circ)$. The azimuth is measured counterclockwise from the X direction to the horizontal component of the momentum vector of the primary cosmic ray. The zenith is the angle between the momentum vector of the incident nucleus and the vertical direction. The core of the shower is located at coordinates $(x_c, y_c) = (67 \text{ m}, 43 \text{ m})$ on the top layer. Top: Central coordinates of the hit scintillating bars and Big Pads of MATHUSLA during the event. Each plane corresponds to a different tracking layer. The third layer of points, from the bottom, are associated to the RPC detector. The axis of the EAS is shown with a continuous black line. Left bottom: Bi-dimensional distribution of the induced signal (in arbitrary units) at the Big Pads of the RPC. Right bottom: Arrival times of the 1st shower particles intersecting the Big Pads of MATHUSLA RPCs. The timing information is given with respect to the arrival time of the first charged particle of the EAS that hit the RPC plane.

which are calculated using the following expressions:

$$x_c = \frac{\sum_{i=1}^{n_{hit}} x_i Q_i}{\sum_{i=1}^{n_{hit}} Q_i}, \quad y_c = \frac{\sum_{i=1}^{n_{hit}} y_i Q_i}{\sum_{i=1}^{n_{hit}} Q_i}. \quad (6.1)$$

Here, i runs over all n_{hit} modules with signal in the corresponding detector plane, (x_i, y_i) is the XY coordinate of the hit i -th detector element and Q_i is the corresponding amplitude of the signal of the Big Pad, where for the scintillating bars, Q_i is set to 1.

We improved the estimates of the EAS core positions by applying a second algorithm that employs the previous core approximations as initial values. In this procedure, for each detector layer, we

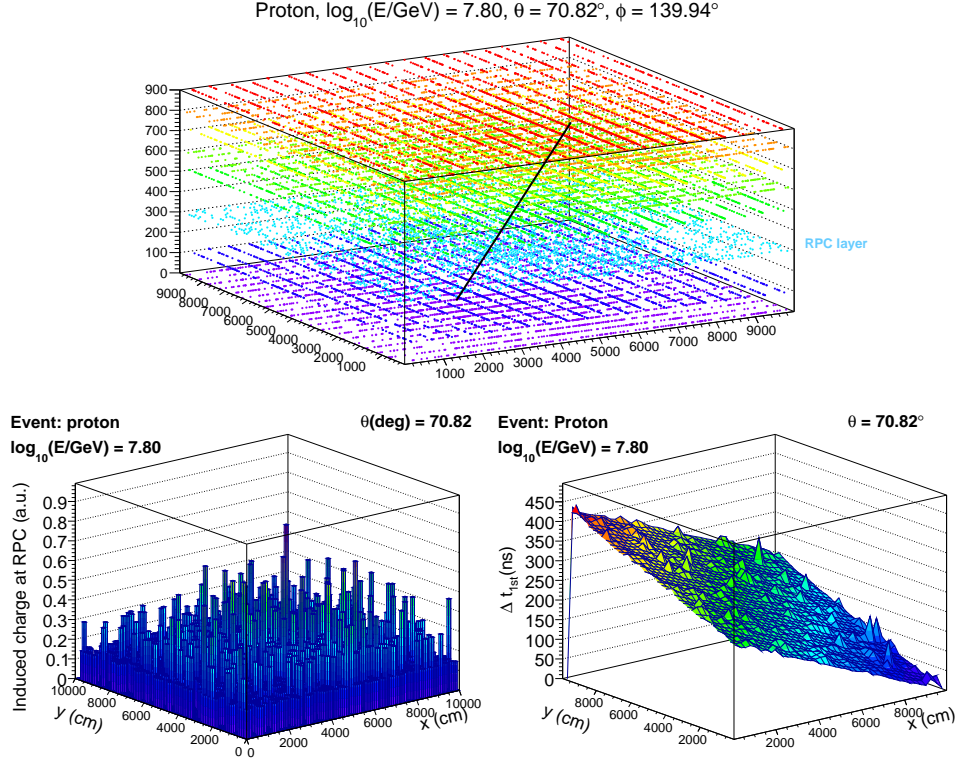


Figure 12. Example of a simulated inclined EAS impinging on the MATHUSLA detector. The event was induced by a primary proton with an energy of $\log_{10}(E/\text{GeV}) = 7.8$ and arrival direction $(\theta, \phi) = (70.82^\circ, 139.94^\circ)$. The azimuth is measured counterclockwise from the X direction to the horizontal component of the momentum vector of the primary cosmic ray. The zenith is the angle between the momentum vector of the incident nucleus and the vertical direction. The core of the shower is located at the coordinates $(x_c, y_c) = (60 \text{ m}, 30 \text{ m})$ on the top layer. Top: Central coordinates of the scintillating bars and Big Pads that are hit. The points in each horizontal plane belongs to a different tracking layer. The third layer of points, from the bottom, are associated to the RPC detector. The axis of the EAS is shown with a continuous black line. Left bottom: Bi-dimensional distribution of the induced signal (in arbitrary units) at the Big Pads of the RPC layer. Right bottom: Arrival times of the 1st shower particles intersecting the Big Pads of MATHUSLA RPCs. The timing information is given with respect to the arrival time of the first charged particle of the EAS that hit the RPC plane.

projected the XY signal distributions on the X and Y axes. The resulting distributions immediately reveal the position of the core, which is located close to the maximum of the projected X and Y histograms. We determine the maximums by fitting the X and Y distributions with lateral functions based on exponential distributions

$$N_{\text{hits},x}(x_i) = \alpha_1 e^{-\beta_1 \cdot |x_i - x_c|}, \quad N_{\text{hits},y}(y_i) = \alpha_2 e^{-\beta_2 \cdot |y_i - y_c|}, \quad (6.2)$$

respectively, using a χ^2 minimisation procedure. In the above equations, $\alpha_1(\alpha_2) > 0$ and $\beta_1(\beta_2) > 0$ are the amplitude and the slope of the projected $X(Y)$ distribution and, as before, (x_i, y_i) is the

coordinate of the i -th detector module in a given detector plane. Finally, x_c and y_c are the positions of the maximums of the projected X and Y histograms, which become our improved approximations to the shower core coordinates. The advantage of this procedure is that it is fast and can be applied for both high and low-energy EAS.

To reduce the effect of fluctuations during the fit, different bin widths are used depending on the fraction of detector elements that are hit, f_{hit} . For the RPC histograms of vertical EAS ($\theta \leq 20^\circ$) we used bin widths of 10 m and 2 m for fractions of Big Pads $f_{hit} \leq 0.2$ and $f_{hit} > 0.2$, respectively. Meanwhile, for $\theta > 70^\circ$, we used only 2 m bins for the RPC distributions.

For the projected histograms obtained from the scintillating detector layers a bin width of 10 m was used for inclined EAS. This bin size was also employed for vertical EAS that induce a fraction of hit scintillating bars $f_{hit} \leq 0.02$. However, for larger f_{hit} values associated with events with the same zenith angle range, the bin width used was 2 m (5 m), if the shortest (longest) dimension of the scintillating bars coincide with the axis of projection used to obtain the histogram.

The bin width selections defined above were chosen to reduce the uncertainties on the core position. We note that a more detailed study would be needed if further improvement is desired.

To illustrate the core reconstruction procedure, we present on the left-hand-side of Figs. 13 and 14 the projected histograms of the signals at the RPC layer of the MATHUSLA detector that were used in the last step of our method to find the EAS core of the vertical and inclined MC events presented in Figs. 11 and 12, respectively. The corresponding fits with the lateral distribution functions of Eqs. (6.2), which provide the final estimations of the EAS core positions, are also displayed in the left of Figs. 13 and 14 together with the best fitting parameters (x_c, y_c) for each event.

From the right-hand-side in Figs. 13 and 14, we found that if there are at least three detector layers where the core position was successfully reconstructed, a fit with a straight line to the corresponding (x_c, y_c, z_c) coordinates of the reconstructed shower core can be applied to get improved positions of the EAS core at each MATHUSLA layer. This procedure could also be used to find the impact points of the shower core in the detector planes where this observable was not successfully reconstructed, provided that the EAS core is inside the instrumented area. This possibility would permit exploiting the tracking capabilities of MATHUSLA, as illustrated on the right-hand side of Figs. 13 and 14, where we show the fits with a straight line to the core positions of the events in Figs. 11 and 12 estimated in each MATHUSLA tracking layer. This technique needs to be further investigated, therefore, it will not be applied in the present analysis.

6.2 Arrival direction of the air shower

In a second stage, the arrival direction of the EAS is estimated using the timing information from the RPC. As a first approximation the direction of the EAS is found from the fit parameters (a_1, a_2, a_3) of a 3D plane to the corresponding arrival time data of the shower front. These parameters are determined by solving the following set of linear equations:

$$a_1 \cdot x_i + a_2 \cdot y_i + a_3 = ct_{1st,i}, \quad (6.3)$$

using the Moore-Penrose pseudoinverse [67]. In the above equation, $i = 1, \dots, n_{hit}$ runs over each detector element with signal in the layer, where n_{hit} is the total number of hit detector modules.

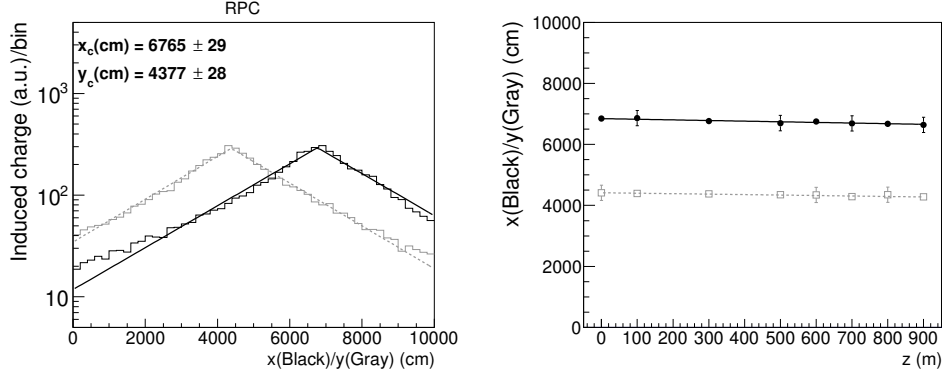


Figure 13. Left: The projected X (black) and Y (gray) distributions of the number of Big Pads at the RPC layer of MATHUSLA for the vertical MC event of Fig. 11. The black and gray lines represent the fits with the formula (6.2) to the X and Y projected profiles of the MC shower event, respectively. The estimated coordinates of the EAS core are shown in the upper left part of the figure. Right: Estimated coordinates of the impact point of the shower core of the MC EAS of Fig. 11 at each of the MATHUSLA tracking layers. The open squares in gray show the respective (z_c, y_c) coordinates, and the black circles, the (z_c, x_c) values of the impact points of the EAS core. The continuous line in black and the dotted line in gray are the corresponding results of the fits with a linear relation to the (z_c, x_c) and (z_c, y_c) data points to improve the estimation of the shower core position.

The arrival time of the first EAS particle to the i -th detector element is represented by $t_{1st,i}$ and the respective spatial coordinates are denoted by (x_i, y_i) , while c is the velocity of the light in vacuum.

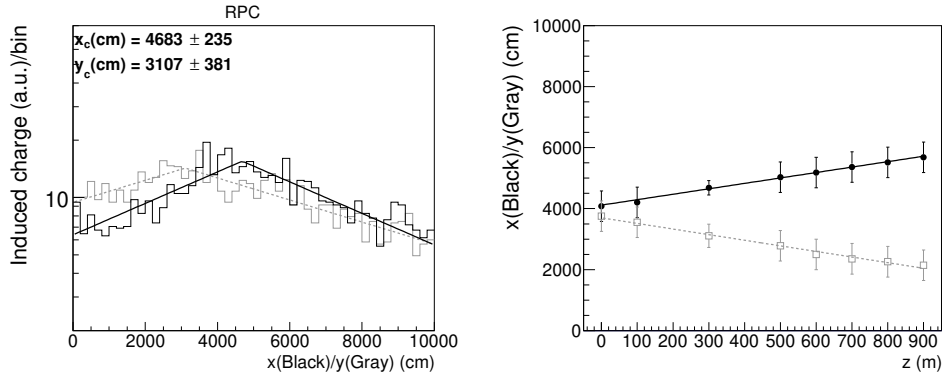


Figure 14. Left: The projected X (black) and Y (gray) distributions of the number of Big Pads at the RPC layer of MATHUSLA for the inclined MC event of Fig. 12. The black and gray lines represent the fits with the formula (6.2) to the X and Y projected profiles of the MC shower event, respectively. Right: Estimated coordinates of the impact point of the shower core of the MC EAS of Fig. 12 at each of the MATHUSLA tracking layers. The open squares in gray show the respective (z_c, y_c) coordinates, and the black circles, the (z_c, x_c) values of the impact points of the EAS core. The continuous line in black and the dotted line in gray are the corresponding results of the fits with a linear relation to the (z_c, x_c) and (z_c, y_c) data points to improve the estimation of the shower core position.

The fit parameters and the arrival direction of the cosmic ray are obtained from the expressions

$$\phi = \arctan(a_2/a_1), \quad (6.4)$$

$$\theta = \arcsin \sqrt{a_1^2 + a_2^2}. \quad (6.5)$$

Here, we are using the CORSIKA definitions for the zenith (θ) and the azimuth (ϕ) angles of the shower axis [60]: θ is the measured angle between the momentum vector of the incident nucleus and the vertical direction, while ϕ is defined as the angle between the horizontal projection of the momentum vector of the primary cosmic ray and the X axis. The angle ϕ is defined as positive for counterclockwise rotations from the X direction. In this case, we need to add π to the result of equation (6.4) if $a_1 < 0$ and $a_2 > 0$, and $-\pi$ when both a_1 and a_2 are negative.

To improve the estimation of the arrival direction of the EAS events, we fit the measured time data with a flat EAS front using the minimum χ^2 method and the previous estimations of θ and ϕ as initial values. We minimised the following expression:

$$\chi^2 = \sum_{j=1}^m \left[\frac{t_{1st,j} - T_0 + (x_j - x_c)n_x/c + (y_j - y_c)n_y/c}{\sigma_t} \right]^2, \quad (6.6)$$

where T_0 , θ and ϕ are the fitting parameters. Here, T_0 is the arrival time of the shower core to the detector layer under consideration, and n_x and n_y are the X and Y components of the normalised vector \hat{n} that is anti-parallel to the momentum of the cosmic ray,

$$\hat{n} = (\sin \theta \cos(\phi - \pi), \sin \theta \sin(\phi - \pi), \cos \theta), \quad (6.7)$$

(x_c, y_c) is the respective position of the EAS core (estimated with the procedure described in section 6.1) and σ_t , the estimated uncertainty in the time measurements, which we conservatively set to 0.5 ns. The index j runs only over the m detector elements that had a signal within a time window of 10^5 ns measured from the first hit recorded in the layer. For the minimization procedure, we used MINUIT [68] from ROOT.

Final approximations of θ and ϕ are obtained by using a cone instead of a plane in the χ^2 fit of the arrival times of the EAS front, which corrects the timing information for curvature effects. In this case, we need to minimise the equation below:

$$\chi^2 = \sum_{k=1}^{m'} \left[\frac{t_{1st,k} - T_0 + (x_k - x_c)n_x/c + (y_k - y_c)n_y/c - r_k \tan(\rho)/c}{\sigma_t} \right]^2. \quad (6.8)$$

In this relation, ρ is the fit parameter that controls the slope of the cone with respect to the plane perpendicular to the shower axis, and r_k is the radial distance of the k -th detector element with signal to the EAS core in shower disk coordinates. This variable is defined as

$$r_k = \sqrt{[(x_k - x_c) - \Delta_k \times n_x]^2 + [(y_k - y_c) - \Delta_k \times n_y]^2 + [\Delta_k \times n_z]^2}, \quad (6.9)$$

with

$$\Delta_k = (x_k - x_c)n_x + (y_k - y_c)n_y. \quad (6.10)$$

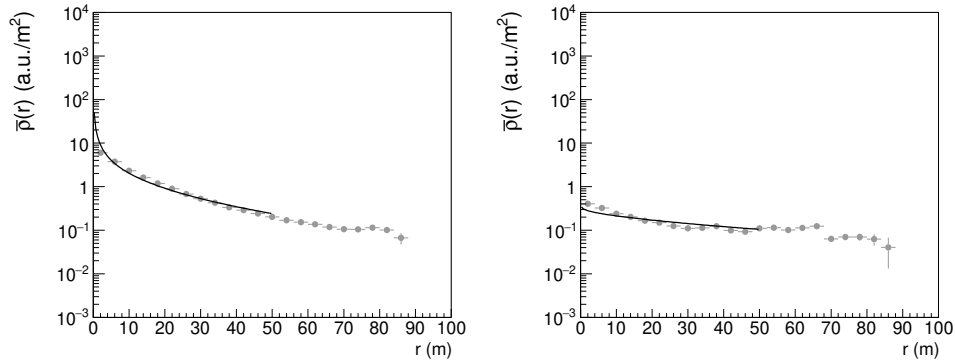


Figure 15. The radial distributions of the mean deposited charge per unit area at the RPC detector of MATH-USLA (at shower disk coordinates) corresponding to the vertical (left) and inclined (right) MC events presented in figs. 11 and 12, respectively. The LDFs are shown with data points, which were fitted with the NKG-like function of Eq. (6.11) (continuous lines).

In equation (6.8), the sum runs only over detector modules with signals at the RPC layer recorded during a time window of 100 ns and 600 ns (taking as a reference the time of the module with the first hit in the detector layer) for vertical and inclined EAS, respectively. The above procedure will be also applied for inclined EAS and timing data from the scintillating detector planes in case of events with charged particle densities below the saturation threshold of the scintillating bars.

6.3 Lateral density distribution of EAS

A useful observable in EAS observatories to study the main properties of cosmic rays is the lateral distribution of particle densities or the lateral distribution function (LDF) at the shower front. Therefore, in the next stage of the EAS reconstruction, the LDF of the event is built using the data from the RPC. For this task, first, we computed the local density of deposited charge, $\rho(r)$, in each Big Pad of the RPC detector. Then, we estimated the radial distances, r , to the EAS core at shower disk coordinates (using the estimated values for the core position and the arrival direction) of the density measurement and, finally, we calculated the mean values of $\rho(r)$ for different bins of r . Here a common bin width of $\Delta r = 4$ m was employed.

The amplitude and the steepness of the radial density distribution of an EAS are considered to be energy and mass composition sensitive parameters of primary cosmic rays, respectively [69, 70]. Therefore, it is necessary to parameterise the LDFs obtained with the RPC measurements of the EAS to explore the sensitivity to the primary energy and the mass of the cosmic-ray nuclei using this information. The parameterization can be achieved by fitting the LDF data with a Nishimura-Kamata-Greisen (NKG) formula [71–73] often used in this context:

$$\rho(r) = A \cdot \left(\frac{r}{r_0}\right)^{s-2} \left(1 + \frac{r}{r_0}\right)^{s-3.5}, \quad (6.11)$$

where A is the amplitude of the LDF, s is a parameter (known as the lateral shower age) that determines the flatness of the distribution and r_0 is a radial scale, whose value we have chosen as the

Molière radius (~ 79 m) at sea level.

Two examples of LDFs obtained from the RPC data for the simulated air showers presented in figs. 11 and 12 are shown in the left and right panels of Fig. 15, respectively. The radial distributions have been fitted with the NKG function (6.11) for $r \leq 50$ m. The fitted functions are also displayed in the above figures. As observed from the plots in Fig. 15, the NKG expression seems to describe reasonably well the LDF of the MC data.

7 Selection criteria

For this work, we have selected a set of quality cuts to reduce the magnitude of the systematic uncertainties in the reconstructed EAS that are used to study the sensitivity of MATHUSLA to high-energy cosmic rays.

We require that the number of elements with signals in each detector layer satisfies the condition $n_{hit} \geq 100$ for vertical events, and $n_{hit} \geq 50$, for inclined EAS. These cuts eliminate low-energy events with large systematic uncertainties. Note that we have reduced the minimum number of hits for inclined events in order to lower the energy threshold in our analysis. In addition, for the analysis of the RPC data, we accepted only EAS that passed the core and arrival direction reconstruction procedure and have reconstructed EAS cores within a central area of $90 \text{ m} \times 90 \text{ m}$ at the RPC layer to avoid border effects. Similar cuts were also applied for the study of inclined events recorded with the tracking layers of MATHUSLA. For vertical data from the scintillating layers, we removed the cut that requires the successful reconstruction of the shower direction at the respective layer, since we did not estimate the shower direction of vertical EAS with these detector elements.

8 Results

8.1 Performance of the RPC

8.1.1 Reconstruction efficiency

The selection-cut efficiency of the proposed RPC layer of MATHUSLA to vertical, $\theta \leq 20^\circ$, and inclined, $\theta = [70^\circ, 80^\circ]$, EAS induced by protons and iron nuclei are presented in Fig. 16. The efficiencies were estimated using our MC simulations generated with QGSJET-II-04. From these graphs, we observe that MATHUSLA reaches maximum efficiency at 10^{14} eV for vertical air showers, and increases to 10^{16} eV for larger zenith angles, which is expected due to atmospheric attenuation of the EAS. We did not simulate a particular trigger condition in our MC simulations. For EAS detection, the RPC is expected to provide the trigger in MATHUSLA, which will be the same for vertical and inclined events. A more detailed EAS analysis with a specific trigger condition for MATHUSLA will be included in a further study.

8.1.2 Systematic uncertainties in EAS reconstruction

The performance of the proposed RPC layer as a cosmic-ray detector was additionally investigated by calculating the systematic uncertainties expected from the EAS reconstruction described in section

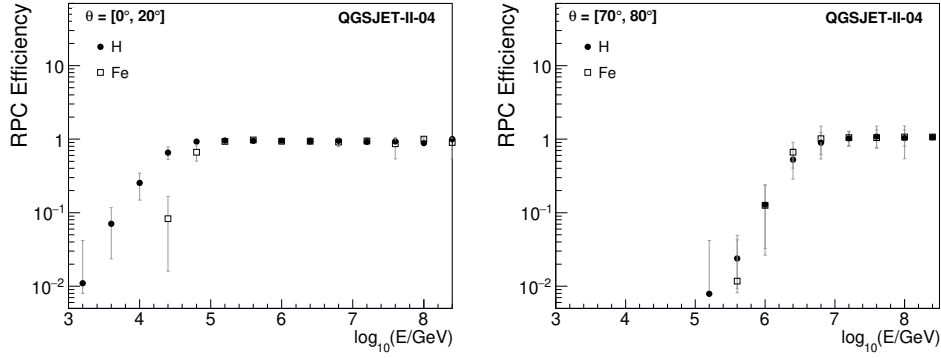


Figure 16. The selection-cut efficiency of the MATHUSLA RPC layer, estimated using the QGSJET-II-04 model, for shower events induced by protons (circles) and iron nuclei (open squares) Left: for vertical EAS with $\theta \leq 20^\circ$ and right: for inclined showers with $\theta = [70^\circ, 80^\circ]$.

6. First, we have estimated the bias and resolution of the arrival angle of cosmic-ray EAS as a function of the primary energy. For this aim, the data is divided in different energy intervals of width $\Delta \log_{10}(E/\text{GeV}) = 0.2$ and for each bin, the distributions of the angular systematic uncertainty are calculated. This systematic is defined as the angle between the reconstructed and true shower axes of the EAS events. Then, the mean and the 68% containment region of these distributions are obtained, which are defined as the angular bias $\Delta\alpha$ and resolution $\Delta\alpha_{68}$ of the RPC layer to EAS events, respectively, and are plotted versus the central energy of the corresponding energy bin. The results are shown in Fig. 17 for vertical (left plot) and inclined events (right graph). The uncertainties were estimated for H and Fe-induced EAS. The left plot of Fig. 17 shows that both $\Delta\alpha$ and $\Delta\alpha_{68}$ diminish with the primary energy from $E = 3.2 \times 10^{13}$ eV to 2.5×10^{17} eV. At low energies ($\lesssim 3 \times 10^{16}$ eV), the angular bias and the resolution vary between 1° and 2° , while at high energies, both uncertainties decrease rapidly to values close to $\sim 0.3^\circ$. On the other hand, the right plot of Fig. 17 shows that for inclined events in the interval $E = [3.2 \times 10^{16}$ eV, 2.5×10^{17} eV], the angular resolution is not as good. At the RPC layer, the bias $\Delta\alpha$ is larger for inclined events than for vertical EAS. From MC simulations, at energies between 3.2×10^{16} eV and 2.5×10^{17} eV, we estimated that $\Delta\alpha = [1.3^\circ, 2.7^\circ]$ and $\Delta\alpha_{68} = [1.3^\circ, 2.9^\circ]$ for inclined showers. In this case, we still observe that both uncertainties decrease at high energies as for vertical EAS, albeit the reduction is not as pronounced as observed for the case of vertical showers.

We also estimated the bias ΔR and resolution ΔR_{68} on the EAS core position expected for the RPC layer at different primary energies. These quantities are defined as the mean and the 68% containment region of the distribution for the distance between the reconstructed and the true shower core locations, respectively, for each energy bin. ΔR and ΔR_{68} are presented in Fig. 18 for vertical and inclined EAS. We employed a bin width of $\Delta \log_{10}(E/\text{GeV}) = 0.2$. The plots were estimated for H and Fe events using QGSJET-II-04. The left plot in Fig. 18 shows that the reconstruction uncertainties for the shower core position of vertical events decrease from a few tens of meters at 3.2×10^{13} eV up to a fraction of a meter between $\sim 10^{15}$ eV and 10^{16} eV, above which the reconstruction

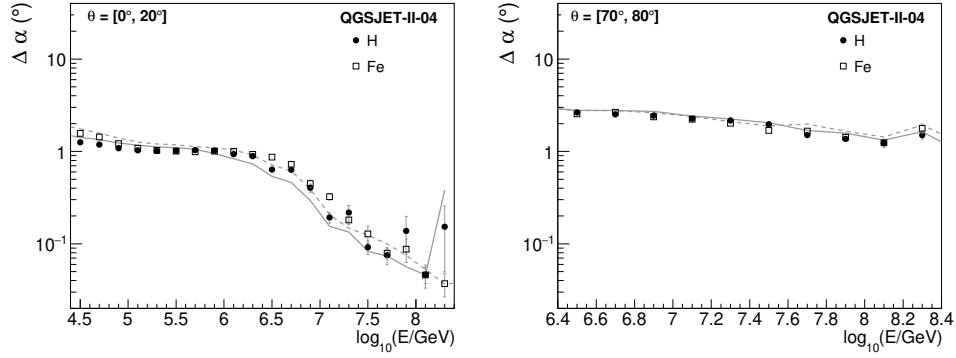


Figure 17. The bias and resolution on the arrival direction of EAS expected for the MATHUSLA RPC layer as estimated from MC events induced by H and Fe nuclei. The simulations were produced with QGSJET-II-04. Quality cuts were applied. Symbols represent the angular bias for protons (circles) and iron nuclei (open squares). The vertical errors are standard uncertainties of the mean. Continuous and dashed lines are used to represent the angular resolutions for H and Fe induced events, respectively. Left: Estimations for vertical EAS with $\theta \leq 20^\circ$. Right: Results for inclined showers within the interval $\theta = [70^\circ, 80^\circ]$.

uncertainties remain almost constant with the primary energy. In particular, the bias (resolution) of the EAS core position at 3.2×10^{13} eV is $\Delta R = 8.6$ m ($\Delta R_{68} = 8.6$ m) and 35.4 m (42.1 m) for H and Fe events, respectively. At energies larger than 10^{15} eV, ΔR and ΔR_{68} are about 0.4 m for vertical showers created by protons and 0.5 m above 10^{16} eV for iron nuclei with $\theta < 20^\circ$.

On the other hand, from Fig. 18, right, we see that for energies greater than 3.2×10^{15} eV, the shower-core bias and resolution for inclined data are of the order of some tens of meters based on our

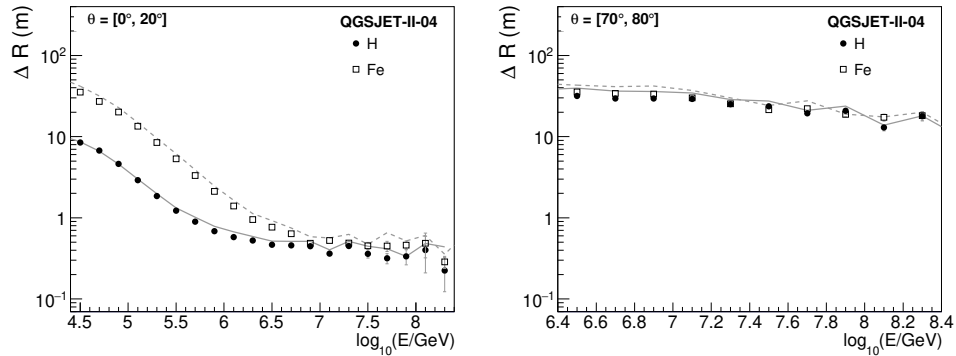


Figure 18. The bias and resolution on the shower core expected for the MATHUSLA RPC layer as estimated from MC events induced by H and Fe nuclei. The simulations were produced with QGSJET-II-04. Quality cuts were applied. Symbols represent the bias on the shower core location for events produced by protons (circles) and iron nuclei (open squares). The vertical uncertainty errors are standard uncertainties of the mean. Continuous and dashed lines are used to represent the core resolutions for H and Fe-induced events, respectively. Left: Estimations for vertical EAS with $\theta \leq 20^\circ$. Right: Results for inclined showers within the interval $\theta = [70^\circ, 80^\circ]$.

shower reconstruction method of MC simulations for the MATHUSLA RPC layer. We also observe that both ΔR and ΔR_{68} are reduced at higher energies, however, their corresponding magnitudes in the high-energy domain do not reach the same values that we found for vertical events. The reason is the reduction in the number of hit Big Pads close to the EAS core for inclined events due to attenuation effects in the atmosphere. For inclined EAS and energies between 3.2×10^{15} eV and 2.5×10^{17} eV, ΔR decreases from 36 m to ~ 14 m, while the core resolution is reduced from 44 m to approximately 16 m.

8.1.3 Fraction of hit Big Pads at the RPC layer

We have also investigated the mean fraction of hit Big Pads f_{hit} at the RPC layer of MATHUSLA that is expected from EAS events of different energies, see Fig. 19. As before, calculations were performed with our MC simulations for vertical and inclined showers, and for protons and iron nuclei as primaries. We used energy bins of size $\Delta \log_{10}(E/\text{GeV}) = 0.2$. For the estimations, we computed f_{hit} event-by-event, then, for a given primary energy bin and cosmic-ray nuclei, we determined the corresponding average values of f_{hit} . From these plots, we can see that f_{hit} increases for vertical showers up to an energy threshold of $\sim 8 \times 10^{15}$ eV at which point the mean hit fraction saturates. For inclined events with $\theta > 70^\circ$, there is no saturation of f_{hit} at least up to energies of 2.5×10^{17} eV.

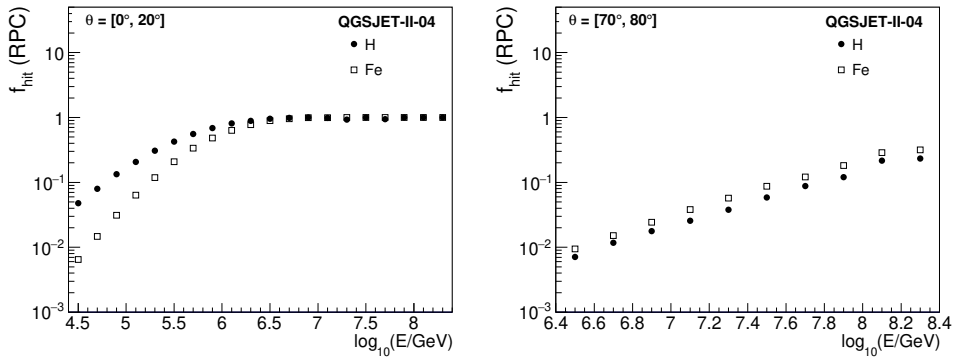


Figure 19. The mean fraction of hits in the Big Pads at the MATHUSLA RPC layer obtained from MC simulations with QGSJET-II-04 for proton (circles) and iron (open squares) cosmic-ray primaries. The results are presented for two zenith angle intervals: left column: $\theta = [0^\circ, 20^\circ]$ and right column: $\theta = [70^\circ, 80^\circ]$. Standard uncertainties on the mean were estimated, but they are smaller than the size of the symbols.

According to Fig. 19, below the energy threshold for the saturation of f_{hit} , the expected fraction of hits is different for proton and iron-induced events. For $\theta < 20^\circ$, f_{hit} is greater for light primaries than for heavy nuclei because proton primaries have a larger production of charged shower particles. For events with $\theta > 70^\circ$, where the atmospheric absorption of the electromagnetic component is more important and the fractional abundance of the muon component increases, the fraction of hits associated with iron events tends to be slightly larger than for proton-induced showers.

The fraction of hits increases with the primary energy of the EAS below the f_{hit} saturation region for both vertical and inclined events. For inclined EAS, this dependence is linear in a logarithmic

scale. These results suggest that f_{hit} could be used to estimate the cosmic-ray energy below the threshold for f_{hit} saturation.

8.1.4 Maximum density of hit particles at the Big Pads due to EAS events

Individual saturation at the Big Pads of the RPC of MATHUSLA is expected to appear for more than $\sim 10^6$ hits of charged particles per module. These densities can be found for air showers of very high energies. Therefore, there could be some EAS energy threshold for which, we would begin to see some saturation of signals at the Big Pads due to shower events. In order to investigate this shower energy threshold, we have used our MC simulations to calculate the mean of the maximum number of hit-charged particles per Big Pad for EAS as a function of the primary energy. The plots for H and Fe-induced showers are presented in Fig. 20 for vertical and inclined events. From the results of Fig. 20, we do not find any potential saturation at the Big Pads due to hadronic-induced EAS in the energy range of interest.

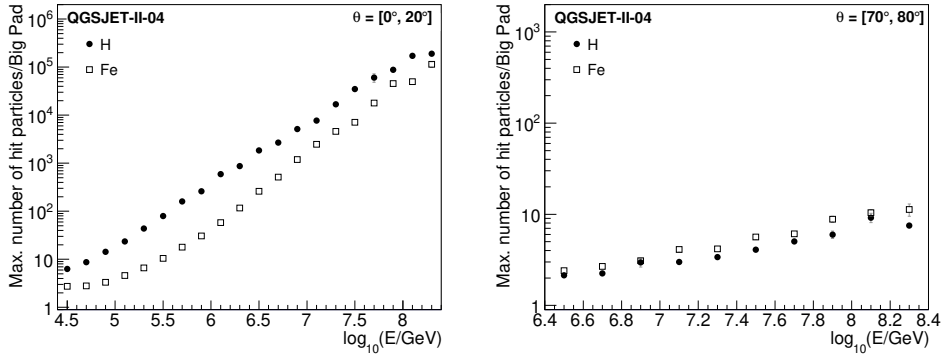


Figure 20. The mean maximum number of charged particles per Big Pad at the RPC layer of MATHUSLA induced by EAS events as a function of the primary energy. The plots were estimated from MC data after applying our selection cuts and employing the QGSJET-II-04 model. Two primary nuclei were simulated: H (circles) and Fe (open squares). MC simulations for vertical EAS ($\theta \leq 20^\circ$) are presented on the left panel and for inclined showers ($\theta = [70^\circ, 80^\circ]$), on the right one. Vertical error bars correspond to statistical uncertainties of the mean.

8.1.5 Spatial structure of EAS at the RPC layer

One of the advantages of instrumenting MATHUSLA with an RPC layer is the possibility of studying the individual morphology of EAS in detail. To illustrate this point, we present in Fig. 21 some MC examples that show the bi-dimensional signal distributions at the Big Pads produced by H and Fe vertical events with shower cores at the centre of the detector for three different primary energies: $\log_{10}(E/\text{GeV}) = 5.0, 5.5$ and 6.0 . The observed patterns in each of these plots show noticeable differences depending on the energy and mass of the primary nuclei. For example, the shower core has a sharper edge, larger amplitudes, and fewer fluctuations at high energies than at low energies. From Fig. 21, we observe that for energies in the interval from 10^5 GeV to 10^6 GeV, the proton-induced EAS are more compact and less clumpy than the showers produced by iron nuclei. The

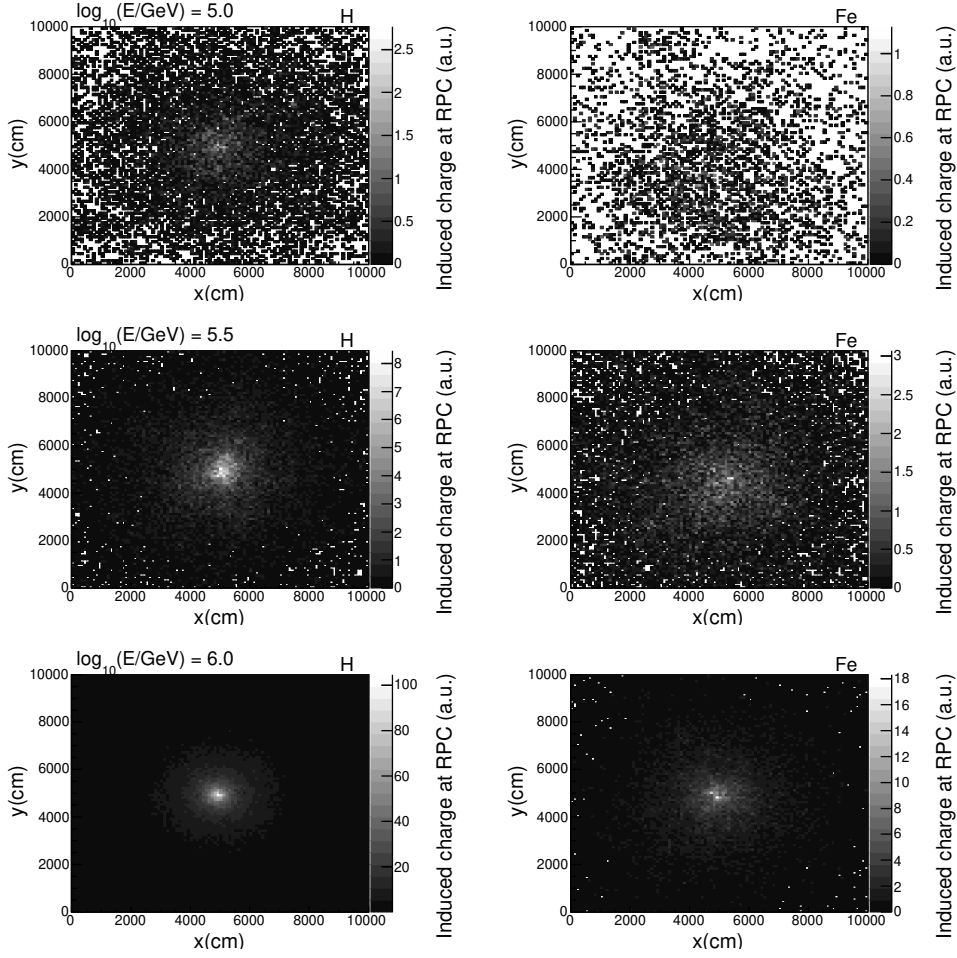


Figure 21. The 2D charge distributions of the RPC MATHUSLA layer for individual MC events with $\theta = 7^\circ$ produced by H and Fe primaries at three different energies. The simulations were produced using QGSJET-II-04. The shower cores hit the center of the instrument on the top scintillation layer. The column on the left was calculated for H primaries, while the column on the right, for Fe nuclei. The top row contains events with energy $\log_{10}(E/\text{GeV}) = 5.0$, the middle row, with $\log_{10}(E/\text{GeV}) = 5.5$ and the bottom row, with $\log_{10}(E/\text{GeV}) = 6.0$. The bins have dimensions $1 \text{ m} \times 1 \text{ m}$.

distinctive morphological features of the EAS measured with the RPC layer are potential observables for distinguishing the nature of the incident cosmic-ray particle and its primary energy.

Another advantage of the RPC layer is that it clearly shows the position of the EAS core at very high energies. For showers produced by iron nuclei of low energies (smaller than a few 10^5 GeV), the EAS core is more difficult to locate from the signal patterns at the RPC because these types of EAS fronts are clumpy, flatter (as we will see later) and are subject to strong fluctuations. This is the reason for the rapid increase of the systematic uncertainty on the shower core position, which we have observed in Fig. 18 for Fe-induced events in the low-energy regime.

Further details about the physical differences of the EAS fronts can be obtained with the RPC

layer from the corresponding measurements of the lateral density profiles, which are presented in the next subsection.

8.1.6 Lateral distribution of EAS from the RPC data

The radial density profile of EAS as measured with the RPC Big Pads of MATHUSLA could be a useful observable for studying primary particles on an event-by-event basis. In Fig. 22, we show the mean radial density profiles, $\bar{\rho}(r)$, calculated from our RPC simulations for proton and iron primaries at different energy ranges and for both vertical and inclined events. The lateral distributions were estimated at shower disk coordinates. For the calculation, we divided the shower front plane in concentric disks of width $\Delta r = 4$ m from $r = 0$ m to 200 m. For each disk with radius r_i , we estimated the average, $\bar{\rho}(r_i)$, of the density measurements of the Big Pads, whose centers were located inside the bin r_i . The local density at each Big Pad was estimated by dividing the respective signal by the projected area of the module $A_{BP}(\theta) = 1 \text{ m}^2 \times \cos(\theta)$, where θ is the zenith angle of the shower axis.

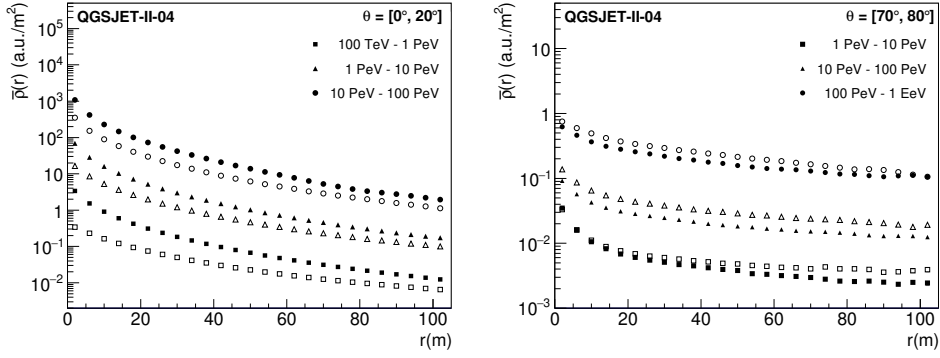


Figure 22. The mean lateral distribution for charged particles of EAS at high energies expected from our simulations of the MATHUSLA RPC detector. On the left, for events with zenith angles in the range $\theta = [0^\circ, 20^\circ]$ for three primary energy intervals: $E = [100 \text{ TeV}, 1 \text{ PeV}]$, $[1 \text{ PeV}, 10 \text{ PeV}]$, $[10 \text{ PeV}, 100 \text{ PeV}]$, the latter are represented by squares, triangles, and circles, respectively. On the right, for $\theta = [70^\circ, 80^\circ]$ and $E = [1 \text{ PeV}, 10 \text{ PeV}]$, $[10 \text{ PeV}, 100 \text{ PeV}]$ and $[100 \text{ PeV}, 1 \text{ EeV}]$. The energy intervals are represented by squares, triangles, and circles, respectively. Solid symbols show the results for EAS induced by protons, and hollow points, for iron nuclei.

It is clear from the plots in Fig. 22 that there are differences among the expected radial density profiles of EAS at the RPC layer depending on the energy, nature and arrival direction of the incident cosmic ray. For example, we observe that the amplitude of the distributions increases with the cosmic-ray energy but decreases with the zenith angle of observation. In addition, the slopes of the density profiles are flatter for low-energy showers than for high-energy showers, as well as for vertical events produced by heavy cosmic-ray nuclei in comparison with vertical EAS due to light mass primaries. From these results, we expect that the RPC data of the lateral density distributions of EAS will provide information on the primary energy and the composition of high-energy cosmic rays. Hence, we should have some shower observables associated to the radial density profiles that could be employed as

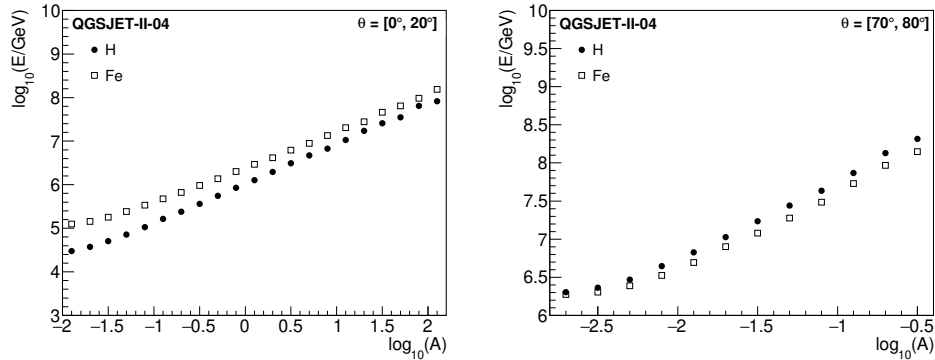


Figure 23. Mean primary energy as a function of the amplitude of the lateral distribution A as defined by equation (6.11) for H (circles) and Fe nuclei (open squares) simulated with QGSJET-II-04. The plot on the left was built for EAS with $\theta \leq 20^\circ$, while the plot on the right was estimated for showers within the interval $\theta = [70^\circ, 80^\circ]$. Vertical error bars represent the uncertainty of the mean. In general, the uncertainties are smaller than the size of the data points.

cosmic-ray energy and composition estimators. We have looked for some of these observables and will present the results in the next subsections.

8.1.7 Potential estimators of the cosmic-ray energy from the RPC data

Using our MC simulations, we investigated the amplitude A of the lateral shower density distributions and the value of the charge density at a fixed radial distance from the centre of the shower core as potential estimators of the primary energy of the EAS events. First, we calculated the dependence of the mean logarithm of the primary energy $\log_{10}(E/\text{GeV})$ on $\log_{10}(A)$ for H and Fe events and vertical and inclined EAS. The results are presented in Fig. 23. We used MC events with $f_{hit} > 0.03$ for vertical data and $f_{hit} > 0.003$ in the case of inclined showers. This selection was chosen to reduce the influence of low-energy events in the results, which have large reconstruction uncertainties.

The plots from Fig. 23 show an approximately linear relation between $\log_{10}(E/\text{GeV})$ and $\log_{10}(A)$ for both proton and iron primaries in the energy region of maximum reconstruction efficiency, which indicates that for vertical and inclined air shower events, the amplitude A can be used to estimate their primary energy. It is important to point out that, according to Fig. 23, left, a mass dependence of the energy calibration function based on the A observable for vertical events is expected to introduce systematic effects when reconstructing the energy spectrum of cosmic rays with this energy scale. Such dependence, however, decreases at large zenith angles, see Fig. 23, right.

As an alternative energy estimator, we also explored the value of the lateral density distribution of the event at a fixed radial distance from the core, in shower disk coordinates. In this case, as an example, we selected the mean density at the radial bin $r = 18$ m, which we denoted as $\rho_{18} = \rho(r = 18 \text{ m})$. The mean logarithm of the primary energy versus $\log_{10}(\rho_{18})$, as computed with MC data, is shown in the plots of Fig. 24 for protons and iron nuclei and within the intervals, $\theta = [0^\circ, 20^\circ]$ and $\theta = [70^\circ, 80^\circ]$. We have applied again the cuts $f_{hit} > 0.03$ and $f_{hit} > 0.003$ for vertical and inclined

EAS, respectively. In both cases, and independently of the primary mass composition, we observe from the plots in Fig. 24 that the curves for the average $\log_{10}(E/\text{GeV})$ vs $\log_{10}(\rho_{18})$ dependence is approximately linear in the energy region of maximum reconstruction efficiency, which implies that ρ_{18} could be also employed as a primary energy estimator. Nevertheless, for vertical EAS, we observe a dependence on the mass of the primary nuclei. This dependence is also observed for values of $\rho(r)$ up to distances of at least $r = 48$ m for $\theta < 20^\circ$.

8.1.8 Sensitivity of the lateral shower age to the mass of the cosmic ray

We have previously noted, in section 8.1.5, that the shape of the lateral distribution in MATHUSLA could be sensitive to the type of the primary particle. One of the parameters of the lateral distribution of EAS that is sensitive to the primary composition is the lateral shower age, s , as defined, for example, in equation (6.11). This parameter measures the flatness of the lateral distribution of the EAS and it is related to the depth of the maximum development of the air shower in the atmosphere, X_{max} , [69, 74]. It is generally known that, at a given energy, light nuclei create air showers with steeper lateral distributions and larger values of X_{max} than heavy primaries. Based on such differences, we say that the EAS associated with the first group are young and the second set, old. On average, the young EAS have relative s values smaller than the old ones. Thereby the age parameter has the potential to be used in mass composition studies (see, for example, [8]).

To investigate the sensitivity of the s parameter to the primary cosmic-ray nature in MATHUSLA, we plot in Fig. 25 the mean age parameter versus the amplitude A as calculated from our MC simulations for the RPC of the apparatus. The plots were computed with our MC simulations for vertical and inclined EAS using both H and Fe primaries. By comparing the graphs for both nuclei for vertical EAS (c.f. Fig. 25, left), we found that there is a mass classification capability in the age parameter above some 100 TeV in MATHUSLA, as the separation of both curves is larger than one standard

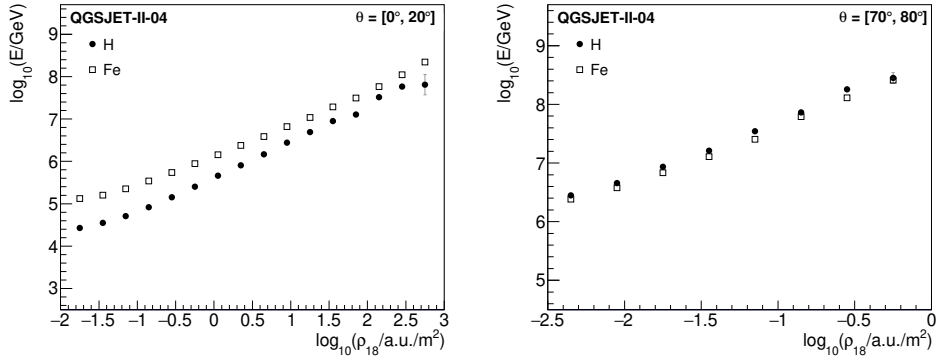


Figure 24. Primary energy as a function of the measured lateral density at the radial bin centred at 18 m with the MATHUSLA RPC layer for EAS due to H (circles) and Fe (open squares) nuclei simulated with QGSJET-II-04 and after applying the quality cuts. The plot on the left was obtained for showers with $\theta \leq 20^\circ$, while the plot on the right was estimated for events within the interval $\theta = [70^\circ, 80^\circ]$. Vertical error bars represent the standard uncertainty of the mean.

deviation in this regime. It is noteworthy that, for vertical events, the mass sensitivity of the age parameter is, in general, enhanced at high energies, at least up to 10^{17} eV, because the uncertainty bars shrink.

For inclined showers, the mass sensitivity of the age parameter in MATHUSLA decrease as seen from the right plot in Fig. 25, since EAS fluctuations are larger and the mean shower age values for H and Fe are very similar. This means that for composition analysis of the primary nuclei with $\theta > 70^\circ$, alternative mass-sensitive parameters must be explored.

8.2 Performance of the scintillating layers

The analyses shown in the previous sections show that the RPC detector layer proposed for MATHUSLA could be well suited for studying high-energy cosmic rays in the experiment. However, the capabilities of the instrument as a cosmic-ray detector could be enhanced by adding data from the scintillating layers of MATHUSLA. Before exploring some of these possibilities, we need to investigate the performance of the scintillating detectors for EAS detection. For this aim, we carried out additional analyses, which will be presented in the following subsections.

8.2.1 Reconstruction efficiency

We start the analyses by investigating the energy range of sensitivity of the scintillating layers of MATHUSLA for cosmic-ray observations. For this task, using MC simulations, we calculated the selection cut efficiency of the scintillating planes as a function of the primary energy. Plots for vertical and inclined events at the top scintillating layer are shown in Fig. 26 to illustrate the results. By comparing these graphs with those in Fig. 16, we observe that the energy thresholds for maximum reconstruction efficiency of EAS at the top scintillating layer are similar to those for the RPC detector plane. In particular, for vertical EAS, we found that the energy threshold of the scintillating detector

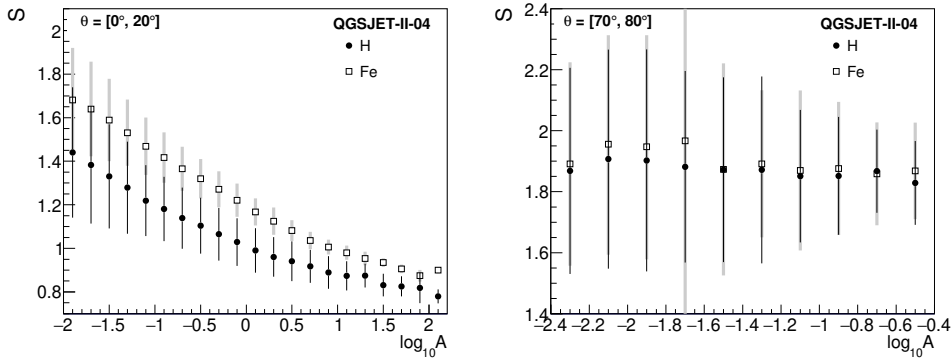


Figure 25. The mean lateral shower age, s , defined in eq. (6.11), against the logarithm of the amplitude A of the lateral density distribution of EAS expected from measurements with the RPC of MATHUSLA. The graphs were estimated from MC simulations using QGSJET-II-04. The circles and open squares represent the results for protons and iron primaries, respectively. The plots on the left are valid for showers with $\theta \leq 20^\circ$, while those on the right, for $\theta = [70^\circ, 80^\circ]$. Vertical uncertainties show the standard deviations of the measurements.

layer is close to 10^{14} eV, while for inclined events, it is approximately 10^{16} eV. Similar conclusions apply to the other MATHUSLA scintillating detector layers since their efficiency plots are similar to the ones presented in Fig. 26.

8.2.2 Systematic uncertainties in EAS reconstruction

We continue the study of the performance of the MATHUSLA scintillating detector layers with an estimation of the systematic uncertainties that could be expected for the reconstruction of EAS events at the scintillating planes using the procedures described in section 6. To evaluate the systematic uncertainties, we have calculated the bias ΔR of the shower core position for vertical and inclined events and the bias $\Delta\alpha$ in the arrival direction of inclined showers. We did not calculate $\Delta\alpha$ for vertical EAS due to saturation problems at some scintillating bars as explained in section 6. In Fig. 27, we present the shower core bias expected for the MATHUSLA scintillating layers vs the primary energy. On the other hand, in Fig. 28, we show the corresponding bias on the arrival direction $\Delta\alpha$ and the core position ΔR for inclined EAS. For the calculation of the bias, we divided the primary energy range in bins of $\Delta \log_{10}(E/\text{GeV}) = 0.2$ and followed the procedure described in section 8.1.2.

In Fig. 27, we note that for vertical events, the bias on the shower core position ΔR at the scintillating layers is less than 41 m for H and Fe primaries, respectively, in the region from 3.2×10^{13} eV to 2.5×10^{17} eV. From the same figure, we also find that the average ΔR decreases in the energy interval from $E = 3.2 \times 10^{13}$ eV to 3.2×10^{14} eV (1.3×10^{15} eV) for proton and iron nuclei, respectively, and then increases at large energies to 41 m. The reduction in ΔR at TeV energies is due to an increment in the number of hit scintillating bars with the primary energy, while the increase appears because at very high energies the EAS core covers most of the surface of the scintillating layers with a large number of tracks (see Fig. 29, left). When all the scintillating layers are covered by

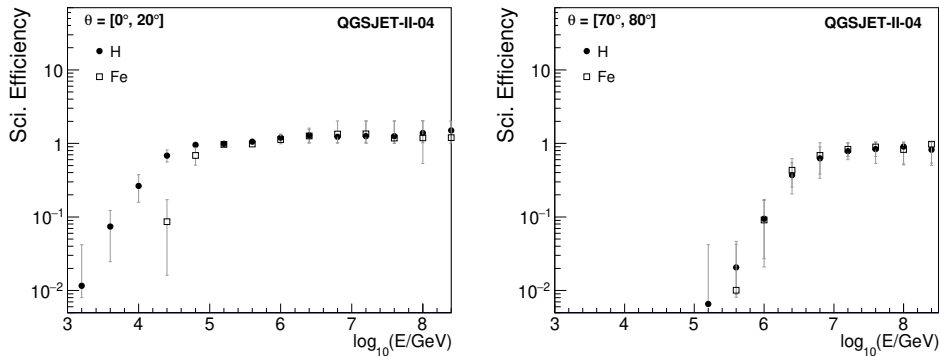


Figure 26. The selection cut efficiency of the top MATHUSLA scintillating layer, estimated using the QGSJET-II-04 model, for shower events induced by protons (black circles) and iron nuclei (open squares) Left: for vertical EAS with $\theta \leq 20^\circ$ and right: for inclined showers with $\theta = [70^\circ, 80^\circ]$. The uncertainty bars show the statistical uncertainties. The upper and lower limits of the statistical uncertainties show the values of the 68.2% and 31.8% containment regions, respectively, of the efficiency distributions at a given energy, which were estimated by dividing the MC data into sub-samples according to the energy interval and calculating the selection cut efficiency for each of them.

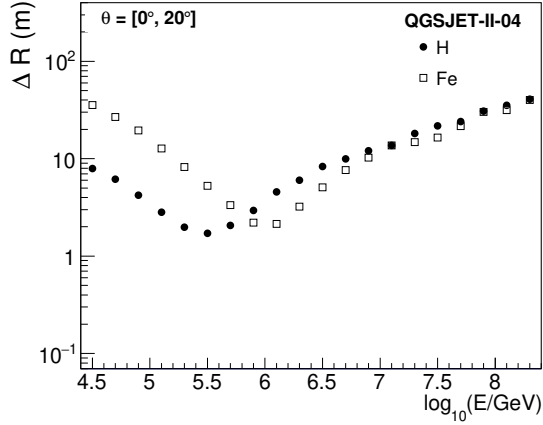


Figure 27. The bias on the shower core position of vertical EAS with $\theta \leq 20^\circ$ expected for the MATHUSLA scintillating layers, as estimated from a selected sample of MC events induced by H (circles) and Fe (open squares) nuclei. The simulations were produced with the QGSJET-II-04 model. Quality cuts were applied. Vertical uncertainty bars represent the statistical uncertainties on the mean. They are smaller than the size of the data points.

tracks it is difficult to locate with sufficient precision the shower core with our reconstruction method (see subsection 6.1). It is worth noting that, from Fig. 27, left, the bias ΔR for EAS produced by iron nuclei is larger than for proton events at TeV energies. This difference is related to the fact that for iron-induced EAS, the shower core is not as well defined as for proton-induced events with the same primary energy.

For showers with $\theta > 70^\circ$ (see Fig. 28, left), saturation effects in the fraction of hit scintillating

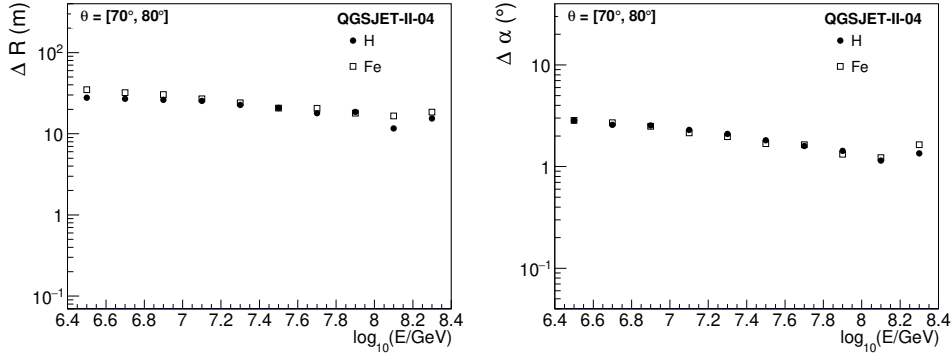


Figure 28. The bias on the EAS core position (left) and arrival direction (right) of inclined showers within the interval $\theta = [70^\circ, 80^\circ]$ expected for the MATHUSLA scintillating layers. The plots were estimated from a selected sample of MC events using H (circles) and Fe (open squares) nuclei as primaries. The simulations were produced with QGSJET-II-04 model. Quality cuts were applied. Vertical uncertainty bars represent the statistical uncertainties on the mean. They are smaller than the size of the data points.

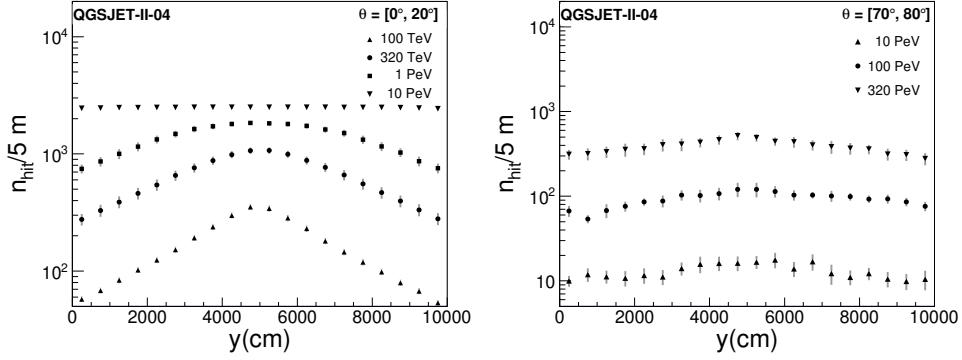


Figure 29. Mean projections on the Y direction of the number of hit bars at the second scintillating detector layer of MATHUSLA (counted from the top of MATHUSLA) expected for proton induced EAS with different energies according to QGSJET-II-04. The shower cores are at the center of the top MATHUSLA layer. Left: Vertical events with energies of 100 TeV (upward triangles), 320 TeV (circles), 1 PeV (squares) and 10 PeV (downward triangles). Right: Inclined EAS with energies $E = 10$ PeV (upward triangles), 100 PeV (circles) and 320 PeV (downward triangles). Projections were build for bins in y of 5 m. Vertical uncertainty bars represent uncertainties on the mean.

bars are no longer important for $E = 3.2 \times 10^{15} \text{ eV} - 2.5 \times 10^{17} \text{ eV}$. However, the quality of the reconstruction of the EAS core diminishes mainly because the shower core is elongated due to the large inclination of the shower axis, and since the lateral particle density is flatter than for vertical EAS (see Fig. 29, right). In addition, the shower fluctuations tend to bias the reconstruction of the EAS core. From Fig. 28, left, we observe that the bias of the EAS core of inclined events decreases with the primary energy. We also notice that at $3.2 \times 10^{15} \text{ eV}$, the systematic uncertainty is equal to 28 m and 35 m for proton and iron events, and decreases to approximately 17 m at $2.5 \times 10^{17} \text{ eV}$.

Finally, in Fig. 28, right, we notice that the bias $\Delta\alpha$ in the arrival direction of inclined EAS decreases from 2.9° at about $E = 3.2 \times 10^{15} \text{ eV}$ up to 1.2° at $2.5 \times 10^{17} \text{ eV}$ at the scintillating layers. In this case, the magnitude and energy dependence of $\Delta\alpha$ is similar for inclined EAS produced by H and Fe primaries.

8.3 Fraction of detector hits per layer

To continue with the study of the performance of the scintillating layers of MATHUSLA for cosmic ray detection, we also estimated the mean fraction f_{hit} of scintillating bars activated in each MATHUSLA detector layer by the EAS at different primary energies using MC data and following the procedure described in section 8.1.3. We used again energy bins of size $\Delta \log_{10}(E/\text{GeV}) = 0.2$. The results for f_{hit} are presented in Fig. 30. From here, we observe an energy dependence of f_{hit} with the primary energy at the scintillating layers analogous to that observed at the RPC system (c.f. Fig. 19). However, for vertical EAS all the detector elements of the scintillating layers are activated at higher EAS energies ($4 \times 10^{16} \text{ eV}$) than for the RPC detector. For inclined EAS, as in the case of the RPC system, we found that f_{hit} for the scintillating layers is not saturated below $2.5 \times 10^{17} \text{ eV}$

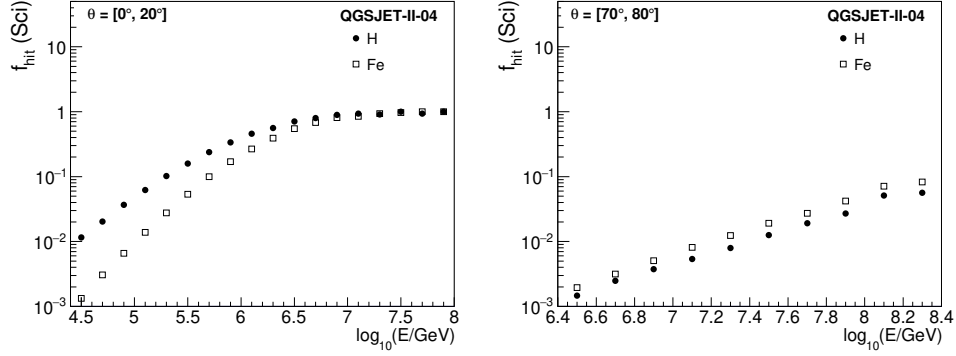


Figure 30. The mean fraction of hit scintillating bars at the MATHUSLA detector layers obtained from the MC simulations with QGSJET-II-04 for proton (circles) and iron (open squares) cosmic-ray primaries. The results are presented for two zenith angle intervals: left: $\theta = [0^\circ, 20^\circ]$ and right: $\theta = [70^\circ, 80^\circ]$. Standard uncertainties on the mean were estimated, but they are smaller than the size of the symbols.

and that f_{hit} increases with the primary energy following a power-law with a small sensitivity to the primary mass.

8.4 Saturation of the scintillation detector layers of MATHUSLA

Another key point in the performance of the scintillating detectors of MATHUSLA studied here is the saturation of the individual scintillating bars. Saturation at each bar occurs, on average, for particle densities greater than $\rho_{th} \sim 5$ charged part./m². Therefore, if the particle density of the EAS exceeds this limit, we will lose information on the distribution of charged particles at the shower front at the scintillation detector layers of MATHUSLA.

To investigate the EAS energy range that will be affected in MATHUSLA by the saturation of the scintillating bars, we have compared the average density threshold of this effect (after applying a geometrical correction factor $1/\cos(\theta)$ due to the inclination of the shower axis) with MC estimations for the lateral distributions of charged particles in air showers (at shower disk coordinates) from primary protons of distinct energies. For vertical events, we used $E = 100$ TeV, 320 TeV, 1 PeV and 10 PeV, while for inclined EAS, we employed $E = 10$ PeV, 100 PeV and 320 PeV. The results, presented in Fig. 31, left, indicate that the saturation of the scintillation bars begins to affect the measurements of vertical EAS induced by protons at energies of ~ 100 TeV near the shower core and that, at higher energies, the area affected by the saturation grows to cover the whole surface of the detector layers at about 10 PeV. In Fig. 31, right, the saturation of the scintillation bars is not dominant in MATHUSLA for inclined EAS with $\theta = [70^\circ, 80^\circ]$ up to primary energies of about 3.2×10^{17} eV.

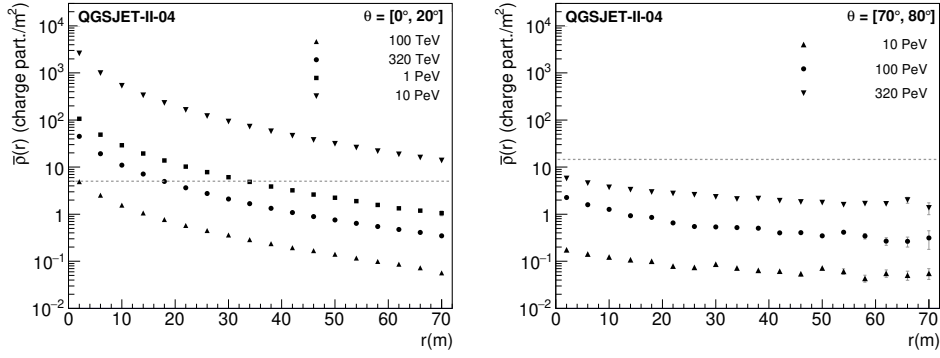


Figure 31. Mean radial densities of charged particles in the EAS front of events produced by protons of different energies. Left: Vertical events with energies of 100 TeV (upward triangles), 320 TeV (circles), 1 PeV (squares) and 10 PeV (downward triangles). Right: Inclined EAS with energies $E = 10$ PeV (upward triangles), 100 PeV (circles) and 320 PeV (downward triangles). Distributions were calculated in shower disk coordinates. The densities were estimated for the MATHUSLA site using QGSJET-II-04. The dashed line shows the value of the average particle density for which the scintillating bars of MATHUSLA are saturated (~ 5 charged part./ m^2 for vertical events and ~ 5 charged part./ $[\cos(70^\circ) \times m^2]$, for inclined showers). Vertical uncertainty bars represent statistical uncertainties on the mean. Bins of 40 m in r were employed to build the plots.

8.5 Muon bundles in MATHUSLA

8.5.1 Events from highly inclined EAS

At large zenith angles, the relative content of muons in EAS becomes increasingly larger due to the stronger absorption of electromagnetic and hadronic particles in the atmosphere. When the arrival direction of the events has zenith angles greater than 65° , muons become the most abundant component of EAS [33]. This phenomenon produces muon bundles [75], which are shower events dominated by multiple muon hits at the detectors. These types of showers are quite interesting to study because muons are sensitive to the physics of hadronic interactions in EAS, the primary energy, and the composition of primary cosmic rays [33]. At the location of MATHUSLA, inclined EAS from primary nuclei with θ between 70° and 80° have an average content of muons of about $(80 \pm 1)\%$ in the region of maximum reconstruction efficiency. This can be seen in Fig. 32, where we present QGSJET-II-04 predictions of the relative ratio of muons to charged particles in hadronic EAS for highly inclined events as a function of the primary energy. Therefore, local measurements with MATHUSLA of the total shower particle content of such events would be quite sensitive to the penetrating component of air showers.

To study the performance of MATHUSLA to these inclined events, we have estimated the expected spectrum and average value of the local muon density D for inclined EAS at the RPC layer using the post-LHC models QGSJET-II-04, EPOS-LHC and SIBYLL 2.3c. The estimations were calculated as a function of the primary energy for H and Fe nuclei. We define D following [75], as the ratio of the total number of particle hits per event to the area of the detector layer. For this study,

we carried out a small production of MC events with EPOS-LHC and SIBYLL 2.3c consisting of 3.3×10^4 and 4.1×10^4 inclined events, respectively, for each primary nucleus following the procedure described in section 5. We also weighted the primary energy spectra of these models to have the same number of events and overall spectral shape (E^{-2}) as QGSJET-II-04. The model predictions for the average values and the spectra of D are shown on the left and right plots of Fig. 33, respectively. We used bin widths of $\Delta \log_{10}(E/\text{GeV}) = 0.2$ and $\Delta \log_{10}(D/\text{m}^2) = 0.32$ for the corresponding plots of the average value of D and its spectrum. From Fig. 33, left, we observe that, at energies above a few 10^{16} eV, the local magnitude of D increases linearly with the primary energy in logarithmic scale, and it is larger for heavy primaries than for light cosmic-ray nuclei. The differences of D for distinct primaries decrease at low energies due to the loss of reconstruction efficiency. We note that the sensitivity of D to the hadronic interaction model is not clear due to the small statistics of the MC data sets. However, it suggests that QGSJET-II-04 could produce inclined events with larger values of D at the MATHUSLA RPCs. Whereas the plot on the right-hand-side of Fig. 33 seems to indicate that the spectra of D for EAS with a high content of muons are higher and harder than for events with a low multiplicity of muons according to the results with QGSJET-II-04, EPOS-LHC [76] and SIBYLL 2.3c [77]. These types of curves could be used to test the predictions of high-energy hadronic interaction models with MATHUSLA RPCs [75]. In particular, if the hadronic models predict fewer muons in EAS above 10^{16} eV than the actual measurements as indicated by some experiments [78], then we may expect that the predicted D spectra, as estimated with a more realistic cosmic-ray composition model, e.g. [79], are smaller than the measured data.

Muon bundles induced by cosmic rays at large zenith angles are expected to have low-particle densities at the MATHUSLA site, with average values smaller than the threshold for density satu-

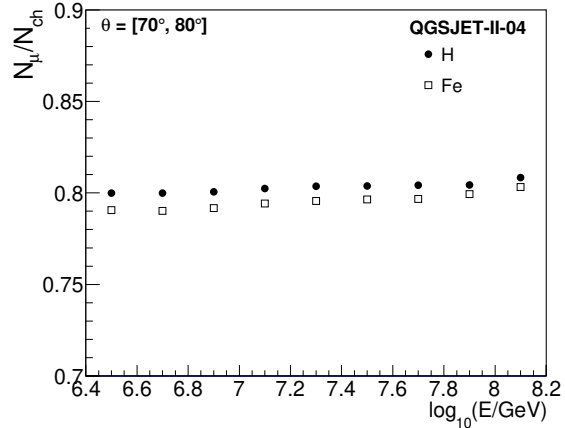


Figure 32. Predictions for the average ratio of muons to the total number of charged particles in hadronic EAS from inclined directions ($\theta = [70^\circ, 80^\circ]$) against the primary energy. The MC simulations were produced for H (circles) and Fe (open squares) primaries using QGSJET-II-04. Standard uncertainties on the mean were estimated and were displayed with vertical error bars, however, they can not be seen because they are smaller than the size of the symbols.

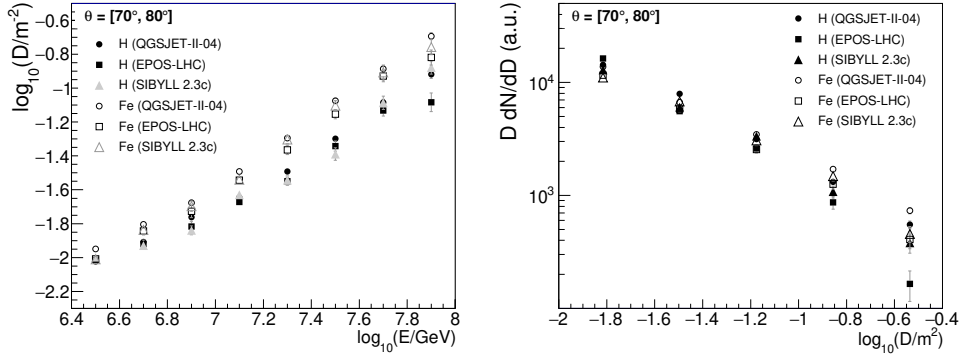


Figure 33. Left: The mean of the local muon density D expected at the RPC of MATHUSLA for inclined events against the primary energy of the EAS according to QGSJET-II-04 (circles), EPOS-LHC (squares) and SIBYLL 2.3c (triangles) predictions for protons (filled symbols) and iron nuclei (hollowed symbols). Vertical bars represent standard uncertainty of the mean. Right: Spectra of the local muon density D of EAS predicted at the RPC of MATHUSLA and multiplied by a factor D . The curves were estimated with the same post-LHC high-energy hadronic interaction models and primary nuclei as in the plot on the left. The primary energy spectra of the models were weighted to have the same number of events and energy spectrum ($\propto E^{-2}$). Selection cuts were applied to the left and right plots.

ration at the scintillating bars for primary energies below a few 10^{17} eV (see Fig. 31). Under these circumstances, MATHUSLA could be used not only to perform independent measurements of local muon densities D but also as a tracking detector to improve the pointing direction of the instrument. According to Fig. 20, fluctuations at the shower front are expected to saturate occasionally some scintillating bars. Despite that, such modules could be removed in a joint EAS analysis involving the scintillating tracking detector and the RPC detector layer.

8.5.2 Events in tandem with the CMS detector

As a stand-alone cosmic-ray detector, MATHUSLA will sample the front of hadronic EAS with its tracking system and the RPC detector layer. However, during the High-Luminosity LHC runs, measurements in combination with the underground detector CMS may also be carried out. This possibility is still under exploration with the CMS group. However, if approved, the CMS detector would make possible EAS measurements of high-energy muons ($E_\mu \gtrsim 61$ GeV for vertical incidence²) in MATHUSLA at different lateral distances on the shower plane, ranging from $r = 0$ m to 168 m, depending of the zenith and azimuth of the shower axis and the impact point of the EAS core on the surface of MATHUSLA. The data may be taken with independent triggers, then time correlations could be searched to find EAS events simultaneously recorded in both instruments. With the CMS data on shower muons, MATHUSLA would have local, high-precision information about the multi-

²Using the analytical formula for the range of muons in matter from [80], cosmic-ray muons of 61 GeV that propagate vertically in 90 m of standard rock will arrive to the top of the CMS cavern with ~ 10 GeV of energy, which is enough to traverse the CMS detector [81]. The value for the muon energy threshold at ground level could be smaller since the material above the CMS cavern is not completely composed of rock [82].

plicity N_μ , radial density ρ_μ , charged ratio μ^+/μ^- , momentum p_μ and energy spectrum of muons for large threshold energies in the EAS front.

For events observed in MATHUSLA and CMS, the most interesting ones would be those in which the shower cores traverse through the instrumented areas of both experiments. The muon data from these golden events would be collected directly from the forward region of the EAS, which is difficult to measure in dedicated particle physics experiments and is not well constrained by hadronic interaction models at high energies. In this case. The statistics are expected to be reduced due to the limited physical area of the CMS detector ($\sim 315 \text{ m}^2$) and the reduced solid angle of observation for golden events. If we only consider the field of view subtended by the RPC detector layer of MATHUSLA from the CMS location, the zenith angle for such events is restricted from approximately 40° to 64° and the width of the azimuth interval to $\approx 71^\circ$ in the CMS reference system (using the geometry presented in figs. 1 and 3). Hence, we could expect an acceptance of around $77 \text{ m}^2 \text{ sr}$ in CMS for these events, which implies a reduction in statistics by a factor of approximately 2.5×10^{-3} with respect to MATHUSLA.

Simultaneous EAS measurements with MATHUSLA and CMS also could help to investigate the connection between hadronic cosmic rays and the properties of muon bundles in underground experiments. These are air-shower events, which produce groups of penetrating muons with variable multiplicity in detectors buried underground under several meters of rock and soil. First measurements of muon bundles were reported by early deep underground experiments like LVD [83], Frejus [84] and MACRO [85]. Detailed studies of muon bundles with underground detectors began with the LEP experiments ALEPH [86], L3+C [87] and DELPHI [88]. The results from the LEP experiments showed that the measured rate of muon bundles with high multiplicity ($N_\mu \gtrsim 100$) from cosmic-ray showers was larger than the predictions of pre-LHC hadronic interaction models [89] like QGSJET01 [90]. In recent measurements at the LHC [91], the ALICE collaboration has shown that the frequency of muon bundle events with $\theta < 50^\circ$ and multiplicities above 100 are in better agreement with QGSJET-II-04 expectations if it is assumed that at primary energies around 10^{17} eV the composition of cosmic rays is dominated by heavy nuclei [92]. Currently, there is no other experiment that confirms the ALICE result. Data from MATHUSLA and CMS in tandem, if they become available, would provide an independent check of the ALICE observations.

8.5.3 Searching for exotic shower events with MATHUSLA

ALICE results on muon bundles allow for the possibility that these underground events are due to exotic mechanisms in EAS [93]. Some theoretical models propose that the high muon multiplicity events reported by ALICE are produced by strangelets, hypothetical nuclear matter composed of doublets or triplets of strange quarks [94], with possible astrophysical origin [95]. In this context, the muon bundles detected by ALICE are thought to be created by a mixture of strange quark matter that loses mass in many successive interactions with air nuclei when penetrating the atmosphere. According to [96], strangelets could induce muon bundles in the atmosphere that could behave as EAS induced by atomic nuclei with an atomic mass larger than that of iron at a given energy. Hence, air shower events produced by strangelets would be characterised by smaller X_{max} values and larger muon contents than hadronic air showers of the same primary energy. By exploiting the differences between exotic

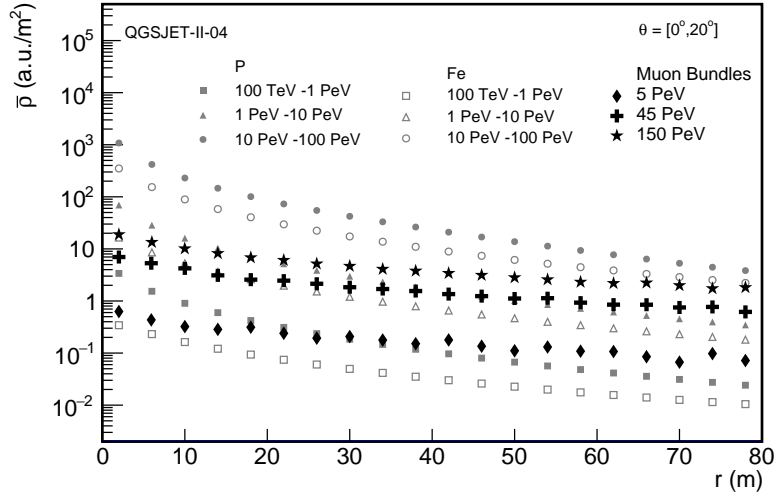


Figure 34. Predictions for the average of the lateral density distributions measured in the RPCs for muon bundles induced by strangelet events in the scenario of [96] for primary energies of 5 PeV (black diamonds), 45 PeV (black crosses) and 150 PeV (black stars) and zenith angles $\theta < 20^\circ$. For comparison, the averages of the lateral density profiles for EAS expected for primary protons and iron nuclei at different energy intervals according to QGSJET-II-04 are presented. Results for hadronic EAS for the energy intervals 100 TeV – 1 PeV, 1 PeV – 10 PeV and 10 PeV – 100 PeV are displayed with gray squares, triangles and circles. For proton and iron nuclei closed and hollow symbols are used, respectively. For hadronic events, we also used EAS with zenith angles below 20° .

and hadronic EAS, it could be possible to perform an event-by-event search for strangelet-induced events in the MATHUSLA cosmic-ray data.

To investigate the potential of MATHUSLA to detect possible muon bundles from an exotic origin in the atmosphere, we simulated the signals of muon bundles at the MATHUSLA RPCs that are created by strangelets and we estimated the lateral density distributions of these events. These profiles were compared with the corresponding predictions for protons and iron-induced EAS in order to look for possible differences in MATHUSLA between exotic and hadronic events. To simulate the production of muon bundles due to strangelets, we took the shower muon content of some QGSJET-II-04 EAS produced by iron nuclei with vertical incidence ($\theta < 20^\circ$) and with primary energies 1 PeV, 10 PeV and 30 PeV. These shower muon particles were passed to our MATHUSLA simulation and reconstruction programs, which are described in sections 5 and 6. Then we applied the selection cuts described in section 7 and, next, with the chosen data we built the average of the muon lateral density distributions of the events at different energies. The magnitudes of the lateral distributions were multiplied by an appropriate factor to reproduce the muon numbers that we should expect in strangelet events that have a similar X_{max} . To find this factor we used the predictions for the mean X_{max} and muon content of EAS induced by protons, iron nuclei and strangelets given in [96]. These

plots indicate that EAS produced by iron nuclei with energies 1 PeV, 10 PeV and 30 PeV have on average the same X_{max} as muon bundles with energies 5 PeV, 45 PeV and 150 PeV, respectively, and that the muon content of these exotic events has approximately 1.3 more particles than Fe induced events with the same primary energy. For QGSJET-II-04, we found $N_\mu \approx 7.3 \times 10^{-2} (E/\text{GeV})^{0.92}$ for Fe nuclei with $\theta < 20^\circ$ and $E = [1 \text{ PeV}, 1 \text{ EeV}]$ at the MATHUSLA detector. Hence, we need to apply a scale factor³ of $1.3 \times (E_{str}/E_{Fe})^{0.92}$ to the lateral density of muons simulated for Fe nuclei of energy E_{Fe} in order to obtain the respective profile for strangelets of primary energy E_{str} .

The average of the lateral density profiles for the simulated muon bundles are presented in Fig. 34 in comparison with QGSJET-II-04 predictions for vertical EAS resulting from protons and iron primaries. We note that the lateral distributions of muon bundles from strangelets decrease less rapidly as a function of r than the respective distributions for hadronic EAS in the scenario described in [96]. A more dedicated analysis is underway. However, this preliminary analysis suggests that MATHUSLA measurements could test the hypothesis on the strangelet origin of the high multiplicity muon bundles observed by ALICE by looking for anomalous events with flatter lateral density distributions than the cosmic-ray-induced EAS. The tests can be more restrictive if these analyses also include the golden events measured in correlation with the CMS detector in the hypothetical case that simultaneous measurements with the underground detector become available. Under these circumstances, by analysing MATHUSLA data from EAS correlated with muon bundles detected at the CMS detector, we could directly verify or discard the exotic nature of these underground events in the context of models like [96].

9 Discussion

The purpose behind the proposal to install an RPC layer in MATHUSLA is to exploit the advantages for EAS studies of combining a large area and full coverage detector that offers a wide dynamical range for charged particle densities, with the benefits of the cosmic-ray tracking capability of MATHUSLA. The RPC layer would provide detailed information of cosmic-ray induced EAS about the spatial and time structure of the shower front in EAS events with different inclinations, while the tracking detector system of MATHUSLA would mainly help to measure the arrival times and radial density profiles of shower particles from inclined EAS. The combination of MATHUSLA with the RPC detector layer would result in an improved tracking detector for studying muon bundles from very inclined directions and for measuring vertical EAS events of TeV energies.

According to the analyses of selection cut efficiency of the RPC layer presented in subsection 8.1.1 the instrument would be sensitive to EAS from primary cosmic rays with energies as low as 10^{14} eV. The particular energy threshold will depend on the selection cuts and arrival direction of the shower. For the selection cuts here employed, the proposed design would have an energy threshold

³The procedure has several drawbacks but it gives us a naive estimation of the effect that we are looking for in MATHUSLA. In [96], for example, the EAS were simulated for the location of the Pierre Auger Observatory, which is situated at an altitude of 1400 m a.s.l. [97]. In addition, for EAS simulations in [96], a modified version of SHOWERSIM [98] was employed. Also X_{max} for hadronic EAS from vertical directions is dominated by photons and electrons and not by muons [33].

of 10^{14} eV to vertically incident cosmic rays, while for inclined events with zenith angles between 70° and 80° the threshold would be 10^{16} eV. For higher energies, EAS detection at the RPC would be restricted by the reduction in the intensity of cosmic rays and the limited sampling size of the detector. This point is illustrated in Fig. 35 that shows the expected event rate of cosmic-ray showers at MATHUSLA as a function of the primary energy considering only events with shower cores impinging on the instrumented area and assuming full detector efficiency. From the rate shown on this plot and considering a collection time of around 3 yr, which is similar to the projected time of the HL-LHC run, we estimate that MATHUSLA would collect ~ 530 air showers with $\theta \leq 70^\circ$ at energies $E > 10^{17}$ eV and almost 52 events with $\theta = [70^\circ, 80^\circ]$ in the same energy range. Therefore, from the previous results, we could expect that the RPC detector layer would be mainly constrained to the primary energy range $E = [10^{14}$ eV, 10^{17} eV] of the cosmic-ray spectrum, i.e. the region around the knee. Based on similar analyses for the MATHUSLA scintillating layers, see section 8.2, we found analogous energy thresholds to those for the RPC detector.

From Fig. 18, 17 and 21, we observe that the proposed RPC layer of MATHUSLA will make possible precise measurements of the core location and arrival direction of vertical events. The per-

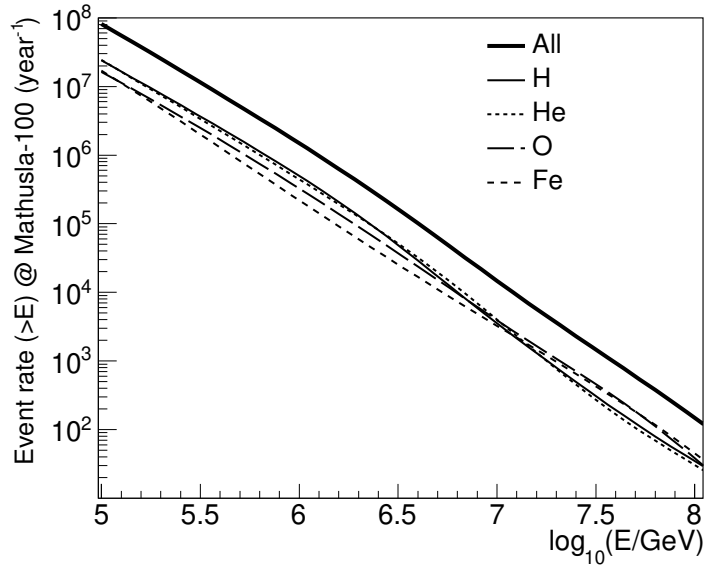


Figure 35. Number of cosmic-ray events per year above an energy E expected at MATHUSLA from the zenith angle interval $\theta = [0^\circ, 90^\circ]$ and for an instantaneous field of view of π sr considering an horizontal detector geometry. These results assume that cores of the cosmic-ray induced EAS are located inside the $100 \text{ m}^2 \times 100 \text{ m}^2$ instrumented area and that the detector has full efficiency. In the calculations, the intensities of cosmic rays for different nuclei were taken from the Global Spline Fit model that was tuned to the latest measurements of cosmic rays in the energy range from 3 GeV to 10^{11} GeV [79]. The black line represents the predictions for the sum of all-particle cosmic-ray nuclei and the colour lines, the expectations for four representative mass groups.

formance of the instrument, however, would be reduced when increasing the inclination of the shower axes of the events. In this case, our estimations for the angular resolution of the RPC layer might be improved by using the tracking capabilities of the MATHUSLA scintillating detectors. This possibility needs further study, but it should apply also to vertical events in the TeV energy regime that have particle densities below the saturation level of the scintillating bars (see section 8.4). A good angular resolution is important when building precise maps of the arrival direction of cosmic rays. These measurements are the basis of studies of the anisotropy [6, 19, 20] and clustering of these particles [99, 100] that are done to get a better understanding of the propagation of this radiation in the interstellar medium and to constrain models on the spatial distribution of galactic cosmic-ray sources [101]. Shower core measurements could also be possible with the MATHUSLA scintillating detectors for TeV showers and inclined events (see figs. 27 and 28). However, we did not observe an improvement here in comparison with the results for the RPC detector.

From figures 11, 12 and 21, we observe that the proposed RPC detector layer of MATHUSLA would provide detailed information on the spatial and temporal structure of the EAS, which could be used to estimate the primary energy of the event, to measure the distribution of charged particles at the shower front, and to investigate the primary mass of cosmic rays. This unique characteristic of the planned RPC detector could help to uncover hints of the internal hadronic processes that occur inside the EAS. Searches for clusters or multiple cores in the shower front of an event [102, 103], as well as measurements of the amount and distribution of charged particles at the forward direction in EAS could be easily done with the RPC layer and would contribute to testing the validity of modern hadronic interaction models at high energies [63, 64, 76, 77].

We found that the amplitude of the lateral distribution of the deposited charge (see Fig. 23) and the value of the charge density at a fixed distance from the core (for example, Fig. 24) are the measured RPC variables that could be used to estimate the primary energy of the EAS. The disadvantage here is that the energy calibration will be model dependent and some influence from the shower fluctuations may be expected in the result because the measurements will be made close to ground level. Notwithstanding, cross-calibration with other cosmic-ray observatories by using the knee feature of the energy spectrum or the intensity of cosmic rays could be exploited to accomplish this task, as it is done, for example, in [79]. Alternative energy calibration methods, like neural networks [104], need to be also investigated. In this case, information on the time structure of the EAS from the RPC and on the spatial structure of the shower front from the scintillating planes may increase the precision in the energy assignment of the shower events.

Another observable that also depends on the primary energy of the EAS is the fraction of Big Pads with signal, f_{hit} , as seen in Fig. 19, left and right. The sensitivity of this observable, however, seems to be constrained to energies smaller than 8×10^{15} eV for vertical showers, since at higher energies, f_{hit} at the RPC is saturated. In contrast, for inclined EAS, we do not see saturation effects on f_{hit} at least up to 2.5×10^{17} eV. In addition, this observable shows a smaller dependence on the nature of the primary particle for inclined events. Thus, f_{hit} could also provide an energy estimate with reduced sensitivity to the mass of the primaries for data with large zenith angles. However, for vertical events, the mass sensitivity of the fraction hit increases. Consequently, the fraction hit from the RPC layer may be also used to study the mass composition of primary nuclei at least in the low-energy regime

($E < 10^{15}$ eV). From Fig. 30, we notice that the scintillating layers of MATHUSLA may also provide an estimation of the primary energy of the events by means of the fraction of scintillating bars with signals, which exhibits a larger energy threshold for vertical EAS (at around $\sim 4 \times 10^{16}$ eV) than the corresponding one for the RPC detector.

For the research of the composition of cosmic rays with the proposed RPC layer of MATHUSLA, a mass sensitive observable could be derived from the analysis of the slope of the lateral distribution of EAS. In this case, the slope of the lateral density of particles can be parameterised in terms of the lateral shower age using an NKG-like function (c.f. section 6.3). Based on our studies in section 8.1.8, the lateral shower age seems to be sensitive to the type of primary nuclei in MATHUSLA (see Fig. 25) and therefore could be employed for analyses of the relative abundances of cosmic rays at least for vertical EAS.

Further sensitivity to the mass composition could be gained by looking at the 2D morphology of the air shower, as measured with the RPC detector, by exploiting the fine-grained spatial resolution of the instrument along with its large coverage. According to our MC simulations, there appear to be mass-dependent differences in the 2D shape of the shower front of EAS as measured with the RPC (see section 8.1.5). Fig. 21 illustrates this point. For example, the clumpiness in iron-induced EAS seems to be more pronounced than for protons of the same energy, and proton-induced events seem to produce more particles in the forward direction than iron nuclei of identical energy. A neural network or deep learning algorithm could be trained with this detailed information on the 2D spatial structure of the EAS to improve the mass classification of cosmic-ray events. In this regard, additional information from the scintillating layers on the morphology of the EAS front could be useful. At TeV energies, the MATHUSLA tracking detector could give additional data on the particle densities at the EAS front in regions outside the shower core, where the scintillating bars are not saturated (see Fig. 31). At higher energies (> 1 PeV), however, the measurements of the lateral particle densities with the tracking detector will be compromised because of the saturation of both the scintillating bars and the fraction of detector elements activated in the scintillating layers.

The role of the bottom tracking layers in MATHUSLA has not been investigated yet, but it may also provide valuable data for the determination of the primary composition of cosmic rays. For example, for inclined EAS the scintillating bars located close to the walls of the pit that are shielded by the surrounding soil and rock could allow the measurement of local muon densities at the EAS front albeit for a narrow range of radial distances.

The cosmic-ray composition in the PeV energy region is an interesting topic. There are still several open questions, which include, for example, the determination of the position of the cut in the spectrum of H + He primaries that is responsible for the structure known as the knee in the all-particle energy spectrum of cosmic rays. The KASCADE detector has located the knee of the H + He mass group at around 4 PeV [9, 10], but ARGO-YBJ recently measured this structure at energies below 1 PeV (~ 700 TeV) [105]. It is not clear yet what is the origin of the discrepancy. It is an unsolved issue that is important to resolve, since the position of the cut depends on the reach of the acceleration mechanisms of cosmic rays [12], the type of source [106], and the leakage of cosmic-ray nuclei from our galaxy [13, 107].

At ground level, on average, almost 80% of the particle content of inclined EAS for primary

energies above a few PeV comprises muons according to our MC simulations with QGSJET-II-04 (see Fig. 32). This suggests that EAS at large zenith angles are basically muon bundles, which could be detected and studied with the scintillating detectors of MATHUSLA. As observed in Fig. 33, left, the RPC layer of MATHUSLA will make possible local density measurements of muon bundles from inclined EAS that together with similar measurements from the scintillating MATHUSLA detectors and the tracking capabilities of MATHUSLA could lead to the design of different tests of high-energy hadronic interaction models (see, for example, Fig. 33, right). This is also an interesting subject, whose study has revealed important discrepancies between the model predictions and data on the shower muon content that indicate problems in the understanding of the physics of hadronic interactions at high energies [78].

Detail RPC measurements on the lateral density distributions of EAS could be also used to look for exotic events (muon bundles) in the background of hadronic showers that could be created by new types of particles such as strangelets in scenarios such as those described in [96] and discussed in section 8.5.3. These primaries could come from stars made of strange quark matter [95, 108, 109].

If we could add to the fine spatial and temporal measurements of the shower front, the muon data from the CMS detector, then correlations between the content of charged and penetrating particles in the shower could be investigated and more interesting analyses of the EAS could be devised based in the local measurements of the density, charge ratio, momentum and energy spectrum of high-energy muons ($E_\mu \gtrsim 61$ GeV) at different radial distances from the shower core, various zenith angle intervals, and distinct primary energies that could serve to give a more comprehensive picture of the hadronic physics in the EAS and also to investigate the primary composition of cosmic rays around the knee.

The idea of probing underground shower muons in connection with EAS at CERN is not new. The L3+C experiment was conceived to investigate this issue [87], and there was also an early proposal at the LHC called ACME, above the ATLAS interaction point that was designed to continue this research [110]. It is worth noting that if we could use the proposed RPC detector layer and the CMS detector at CERN, it could also be possible to study the relation between underground muon bundles and EAS induced by cosmic-ray primaries of different energies and nuclear masses and to put limits to strangelets scenarios. It has been speculated that such particles may also produce large multiplicity muon bundles in underground detectors [94]. Correlated measurements between the MATHUSLA RPC layer and the CMS detector in this context would enable exploring these exotic physical possibilities and put limits on them. The investigation of these subjects is attractive, as their existence may reveal new kinds of astrophysical objects in the universe, new states of nuclear matter, and a new type of astrophysical radiation.

From this work, the cosmic-ray physics targets for the scintillating layers of MATHUSLA are mainly the study of the energy spectrum and composition of cosmic rays between 10^{14} eV and 10^{17} eV, the analysis of muon bundles, tests of hadronic interaction models of high energy with the muon content of inclined EAS and studies of the skymap distribution of the arrival directions of cosmic rays. The energy range from 10^{14} eV to 10^{15} eV in the energy spectrum of cosmic rays is very interesting as it has not been completely explored because it is located at the limit where direct and indirect detection techniques of cosmic rays can be applied. If the CMS experiment also joins

this quest, the data from MAHUSLA and CMS would allow looking for connections of underground muon bundles and hadronic shower events. Even more, the CMS-MATHUSLA data on cosmic rays would make it possible to explore the spectrum, local density, and charge ratio of shower muons of high energy at different lateral distances from the EAS core, including the forward region.

9.1 Comparison with other EAS detectors

MATHUSLA will be a new type of instrument to investigate in detail the temporal and spatial structure of EAS at ground level and to study the physics of cosmic rays for primary energies between 100 TeV and 100 PeV. The detector will sample a large area ($\sim 10^4 \text{ m}^2$) of the EAS front with an RPC plane characterised by a huge coverage ($\sim 81\%$) and an excellent spatial resolution ($\sim 1 \text{ m}^2$ using the Big Pads, and smaller employing the RPC strips). It will also use a tower of scintillating detector planes, which will provide complementary information about the physical size and shower core location of vertical EAS at TeV energies and, for inclined events, their arrival direction using the tracking properties of the MATHUSLA detector. There is a possibility that the CMS detector could join the MATHUSLA cosmic-ray program. If so, for some shower events measured during the high-luminosity runs at the LHC, the CMS underground detector would provide additional data on the local multiplicity, momentum, and charged ratio of high-energy muons at the EAS front. Such a combination of air shower detectors has not existed to date in a single EAS experiment, and given the characteristics of MATHUSLA, it could provide novel information about the characteristics of the air showers induced by cosmic rays and put limits on the hadronic physics involved.

In table 5, we show a comparative table of the physical extension (A), sensitive area (A_s), and size of the detector modules (A_{unit}) of the MATHUSLA RPCs and the detection systems of other air showers installations that are optimised for cosmic-ray studies within the 10^{14} eV to 10^{17} eV energy range: LHAASO [111], HAWC [112], ICETOP [104, 113, 114] and TALE [115–117]. We also include details on ARGO-YBJ [105, 118], which is the predecessor of the proposed RPC layer of MATHUSLA, and KASCADE [119], which was an important air shower detector array dedicated to studying the electromagnetic, muon and hadron components of EAS at ground level with the objective of investigating the energy spectrum and composition of cosmic rays from 1 PeV up to 100 PeV. KASCADE incorporated several particle detector systems: an array of scintillating detectors, a muon tracking detector, and a central calorimeter.

From the list in table 5, we can observe that only the water Cerenkov detector of LHAASO, the central detector carpet of ARGO-YBJ and the central calorimeter of KASCADE have a large coverage. The water Cerenkov array of LHAASO has a 100% coverage and a large detection surface. However, its spatial resolution is not comparable to the one expected for MATHUSLA. The central carpet of ARGO-YBJ had a coverage of 93% and a spatial resolution of 1.7 m^2 (size of the Big Pads), but a physical area that was a factor of 0.58 that of MATHUSLA. With regard to KASCADE, the central calorimeter had a coverage close to 98% and better spatial resolution (0.06 m^2), but a size 31 times smaller than the one foreseen for the MATHUSLA detector. From these comparisons, we can conclude that MATHUSLA would provide improved time-spatial measurements of the EAS front with large coverage and physical area; conditions that have not simultaneously existed in previous or existing air shower facilities yet.

Table 5. Comparison with other air shower detectors

Experiment	A (10^4 m^2)	A_s (10^4 m^2)	A_{unit} (m^2)	Coverage (%)
MATHUSLA	1	0.81	1	81
HAWC [112]				
<i>central water cherenkov detector array</i>	2.2	1.26	41.9	57.07
LHAASO [111]				
<i>water cherenkov detector array</i>	7.8	7.8	25	100
<i>e.m. detector array</i>	10^2	0.52	1	0.52
<i>muon detector array</i>	10^2	4.22	36	4.22
ICETOP/ICECUBE [104, 113, 114]				
<i>ice cherenkov detector array</i>	10^2	0.042	2.6	0.42
TALE/Telescope array [115–117]				
<i>TALE e.m. detector array</i>	7×10^3	0.031	3	4.4×10^{-4}
<i>TA e.m. detector array</i>	7×10^4	0.152	3	2.2×10^{-4}
ARGO-YBJ [105, 118]				
<i>central carpet</i>	0.58	0.54	1.7	93.00
<i>guard ring</i>	1.1	0.0043	1.7	0.39
KASCADE [119, 120]				
<i>e.m. detector array</i>	4	0.049	1.94	1.23
<i>muon detector array</i>	4	0.062	3.24	1.56
<i>muon tracking detector</i>	0.024	0.013	8	53.87
<i>central calorimeter</i>	0.032	0.031	0.06	97.66

In comparison with the EAS facilities described above, except ARGO-YBJ and HAWC, MATHUSLA will measure only one shower component, i.e., charged particles. This can be seen in table 6, where the EAS observables accessible to LHAASO, HAWC, ICETOP, TALE, ARGO-YBJ and the KASCADE experimental facilities are compared with MATHUSLA. We also included TAIGA-HiScore [121, 122] in the list. From table 6, we observe that MATHUSLA has the disadvantage that it could not measure the muon component or the longitudinal profile of the EAS event-by-event. This restriction implies a smaller sensitivity to the mass of the primary particle and a larger dependence of the energy scale on the primary composition. However, by using good resolution measurements of other shower properties with the MATHUSLA RPCs, such as the arrival times of the shower front, the shape and the amplitude of the lateral density profile, the 2D spatial structure of the EAS and the fraction of hits, along with complementary data from the scintillating detector planes, the composition dependence of the energy assignment could be reduced and the mass sensitivity increased in MATHUSLA. The experiment may also use local muon measurements from the CMS detector. If this is the case, we could look for correlations between underground muon data from CMS and EAS events observed with the detector planes of MATHUSLA. These golden events would allow MATHUSLA to study the mass composition of cosmic rays below and above the energy region of the knee. The disadvantage of MATHUSLA in this regard will be the statistics since the measurements will be restricted to the data-taking periods of CMS for the HL-LHC.

There are several open questions at energies just below the knee of the cosmic-ray spectrum, such as the shape of the energy spectrum of iron nuclei [9, 10, 123] and the discrepancy between ARGO-

Table 6. Experimental comparison

Experiment	Energy range (PeV)	Altitude (m a.s.l.)	Size (10^4 m^2)	EAS component	Energy calibration
MATHUSLA	$10^{-1} - 100$	374	1	N_{ch}	Hadronic model
HAWC [112]	$10^{-3} - 1$	4100	2.2	N_{ch}	Hadronic model
LHAASO [111]	$10^{-1} - 10^3$	4410	100	N_{ch}, N_e, N_μ, N_h	Cherenkov light
ICETOP/ICECUBE [104, 113, 114]	$0.25 - 10^3$	2835	100	N_{ch}, N_μ	Hadronic model
TALE/Telescope array [115–117]	$2 - 2 \times 10^3$	1400	7×10^4	N_{ch}, N_e	Cherenkov/Fluorescence light
TAIGA-HiSCORE [121, 122]	$0.2 - 3$	675	50	N_e	Cherenkov light
ARGO-YBJ [105, 118]	$0.0003 - 3$	4300	1.1	N_{ch}	Hadronic model
KASCADE [119]	$1 - 100$	110	4	N_{ch}, N_μ, N_e, N_h	Hadronic model

YBJ [105] and KASCADE [9, 10] results on the location of the knee feature in the spectrum of light elemental nuclei. Measurements in this energy range are difficult for experiments like KASCADE, ICETOP, TALE, and TAIGA that have an energy threshold near the knee due to limitations of the indirect cosmic-ray detection techniques, and for instruments like HAWC and ARGO-YBJ, where the sensitivity ends at energies near the location of this feature because of restrictions of the size of the detectors. Generally, in order to achieve lower primary energy thresholds the large detector arrays must be located at high altitudes. LHAASO is one of a new generation of EAS detectors located at high altitudes that will allow for cosmic-ray composition studies from 10^{14} eV up to 10^{18} eV covering the knee region. Cosmic-ray measurements with EAS detectors starting at the TeV region are scarce, hence MATHUSLA could become very useful to confirm or complement the measurements on the mass composition of cosmic rays performed with high-altitude EAS observatories such as LHAASO.

MATHUSLA is not located at a high altitude as HAWC or LHAASO, as seen in table 6. This means that shower fluctuations will have a stronger influence on the energy determination of the primary nuclei in MATHUSLA. However, this issue is not expected to spoil studies of the energy spectrum of cosmic rays. Analyses with KASCADE have shown that the spectrum can be investigated even at an altitude close to sea level [9, 10].

LHAASO [111] and ICETOP/ICECUBE [104, 113, 114] are some of the present EAS experiments that have the capabilities to measure the muon component of hadronic EAS in the PeV region (see table 6). LHAASO contains an underground muon detector array, which when completed will cover an enormous surface 100 times larger than the physical area of MATHUSLA. This detector system will be able to perform measurements of muon densities ($E_\mu > 1 \text{ GeV}$) at different lateral distances at the EAS front and from distinct zenith angles [124]. ICETOP can make density measurements of GeV muons in EAS for primary energies between $\sim 1 \text{ PeV}$ and $\sim 100 \text{ PeV}$ and radial distances between 600 m and 800 m for vertical showers using a 1 km^2 detector array [125]. KASCADE also provided local density measurements of muons at different energy thresholds, radial distances, and zenith angles for cosmic-ray-induced EAS of energies from 1 PeV to 100 PeV. One of the KASCADE muon detector systems was a shielded scintillating detector array, which had an area of 4 times larger than MATHUSLA and allowed to get muon data at energies $E_\mu > 230 \text{ MeV}$ [69]. MATHUSLA will not have a muon detector system. However, if the CMS experiment could be added to the MATHUSLA cosmic-ray studies, the correlation with underground measurements of shower

muons would provide relevant information about the high-energy muon component ($E_\mu > 61 \text{ GeV}$) in EAS in the PeV energy region. The disadvantage of this combined detection system would be that the muon data would be restricted to limited radial distances, which would depend on the impact point of the shower core at the ground and the arrival direction of the EAS. In addition, the CMS data would be available only for events registered during the running time of the underground detector. The correlation of MATHUSLA with CMS would have the advantage that could make possible not only measurements of the local densities and multiplicities but also of the energy spectrum and charge ratio of high-energy muons event-by-event, even from the forward region of the hadronic collision. No EAS facility has such possibilities at the moment. If the MATHUSLA detector becomes a reality and the CMS muon data is added, the correlations of underground shower muons and surface EAS measurements could provide new insights into air shower physics at very high energies.

Underground measurements of high-energy shower muons are not possible for the experimental facilities of table 6, but it could be possible in MATHUSLA with CMS. At the moment, there is only one underground EAS experiment, which has a similar energy threshold for shower muons as CMS, it is called EMMA and it is located in the Pyhasalmi mine, Finland under 75 m of rock [126–128]. EMMA is aimed to study underground muon bundles and the composition of cosmic rays in the 1 PeV–10 PeV interval. It consists of an array of eleven tracking muon detectors, each with an area of 15 m². The experiment has an effective area of 100 m², which is similar to the physical area of CMS, but EMMA offers a larger monitoring time and, therefore, a larger exposure⁴ than CMS [128]. CMS, however, has the advantage that it is a high-precision muon detector, has 100% coverage, and can provide additional event-by-event information about shower muons than EMMA, such as information about the energy spectrum and charge ratio of these penetrating particles. The MATHUSLA and the CMS measurements could be correlated with EAS data measured at ground level to increase the reach of the air shower investigations, an option that is not possible at the moment in EMMA.

MATHUSLA will also have tracking capabilities that are not available in other EAS experiments. The tower of scintillating layers and the RPC detector plane of MATHUSLA could work as a giant EAS tracking detector for charged particles in the EAS, albeit with some restrictions due to saturation effects in the scintillating bars for vertical events above 10 PeV. An instrument such as MATHUSLA is unprecedented in the study of cosmic rays. It could help, for instance, to improve the estimation of the arrival direction of EAS and to look for point sources in the small-scale anisotropy maps of cosmic rays. The main motivation for these studies comes from the possibility that there could exist nearby sources of cosmic-ray nuclei that suffer small deviations in the interstellar magnetic field before arriving to the Earth and/or could be emitting detectable neutral particles, such as high-energy neutrons (at $E \sim 100 \text{ PeV}$ one n has a decay length of 1 kpc) or gamma-rays [99, 100, 129]. The presence of such sources might explain the existence of small-scale anisotropy or clustering of events in the maps of the arrival direction of cosmic rays. This is an interesting possibility that has been barely explored at energies above the knee because it requires not only a good angular resolution but also enough statistics to compensate the low-intensity flux of cosmic rays at this energy regime. The presence of nearby

⁴The exposure is the effective area of the detector multiplied by the effective time of observation and the solid angle covered by the experiment.

accelerators of very high-energy cosmic rays is still an open question in astrophysics and one that it is important to verify or constrain with the MATHUSLA detector’s capabilities. A nearby source could be an interesting laboratory to study the particle physics acceleration at high energies and could help to study the propagation of cosmic rays in the galaxy, to identify the types of cosmic accelerators, etc.

By looking at other particle tracking detector systems in different EAS experiments, we can also envisage additional studies for MATHUSLA. KASCADE, for example, was equipped with two tracking detector systems for shower muons and hadrons but smaller in size than MATHUSLA. In KASCADE, the muon tracking detector was employed for measurements of the lateral distributions of muons ($E_\mu > 800 \text{ MeV}$) [130], muon production heights and muon multiplicities [131]. The hadron tracking detector was dedicated to measuring the deposited energy, multiplicity and arrival directions, local densities and geometric distributions of hadrons ($E_h > 10 - 50 \text{ GeV}$) in the EAS front [132–135]. These tasks were specialised for the muon and hadron components of the EAS and some of them could also be employed for MATHUSLA, for example, for shower muons of inclined EAS.

For muon bundle studies above 1 PeV and zenith angles $> 30^\circ$ [136], there is a large facility called NEVOD-DECOR located in Moscow, Russia [75]. The experiment consists of a Cherenkov water calorimeter (NEVOD) with a volume of 9 m (height) \times 9 m (width) \times 26 m (length) and a 70 m² tracking detector (DECOR) composed of eight modules of streamer tubes, which covers three of the lateral surfaces of the NEVOD detector. It has a spatial resolution of 1 cm and an angular precision of 1° for individual tracks. In comparison, the tower of scintillating layers of MATHUSLA of the intermediate and upper detector layers would have a vertical dimension similar to the NEVOD-DECOR experiment, but a larger sensitive area, which could reduce the statistical uncertainties on the measurements of the local densities of muon bundles. This advantage of MATHUSLA could help to improve the investigations of muon bundles between 1 PeV and 1 EeV. Particularly important are the measurements close to the ultra high-energy regime, where a muon excess has been reported in EAS from inclined directions by cosmic-ray detectors like the Pierre Auger observatory [97]. The origin of this anomaly has not yet been well understood and is still under investigation by different experimental collaborations [78]. In addition, MATHUSLA could also provide additional spatial-time information on a larger scale than the NEVOD-DECOR experiment that could help to study the structure of the EAS front. However, the NEVOD detector can make calorimetric measurements of the shower for muon bundles from inclined directions [137], which MATHUSLA cannot. In this comparison, we have not considered the bottom scintillating layers of MATHUSLA, which could increase the effective area of the detector and provide additional data of inclined events, for example, information on high-energy muons by using the surrounding rock as an absorbing layer.

In table 7, we summarise the shower core and angular resolutions for vertical EAS in ARGO-YBJ, HAWC, ICETOP, TALE, the main array of KASCADE and MATHUSLA at about 1 PeV for vertical events. From these values we note that the core resolution expected for MATHUSLA is comparable to LHAASO, ARGO-YBJ and KASCADE, and better than HAWC and ICETOP. While the angular resolution is similar to the resolution of ICETOP. It also appears to be better than the TALE angular resolution, but worse than that for the experiments ARGO-YBJ, HAWC, KASCADE and LHAASO. We expect to be able to improve the shower core and angular direction precision of

Table 7. Core and angular resolution of EAS in different cosmic-ray experiments at 1 PeV in comparison with MATHUSLA.

Experiment	Core position	Pointing direction
ARGO-YBJ [70]	$\lesssim 2$ m	$\lesssim 0.3^\circ$
HAWC [112]	$\lesssim 8$ m	$\lesssim 0.3^\circ$
ICETOP/ICECUBE [104]	$\lesssim 16$ m	$\lesssim 0.7^\circ$
TALE (Telescope array) [116]	–	$\lesssim 5^\circ$
KASCADE main array [119]	$\lesssim 1.5$ m	$\lesssim 0.25^\circ$
LHAASO [138]	$\lesssim 2.5$ m	$\lesssim 0.16^\circ$
MATHUSLA-100	$\lesssim 2$ m	$\lesssim 1^\circ$

MATHUSLA. For this, we employed simple EAS reconstruction techniques, which could be further refined. By exploiting the fine granularity of the RPC detector improvements are also possible. In addition, we are investigating alternative EAS reconstruction methods.

10 Conclusions

MATHUSLA comprises a large tower of tracking detector planes⁵ that will monitor a volume of $25 \text{ m} \times 100 \text{ m}^2$ to look for signals of exotic long-lived-particles produced at the interaction point of the CMS detector during the High-Luminosity LHC runs. The instrument can also serve as an extensive air shower detector to primary cosmic rays in the energy range from 10^{14} eV to 10^{17} eV. The lower limit might be relaxed by reducing the number of hits required by the selection cuts. This way MATHUSLA will enable measurements of the energy spectrum of TeV cosmic rays as well as of muon bundles associated with inclined events. Adding an RPC layer significantly enhances the capabilities of MATHUSLA for cosmic-ray physics. The RPC detector system would provide fine space-time information about the EAS front at ground level that can be used to calibrate the primary energy of the event and study the mass composition of cosmic rays, as well as the structure of the EAS front and the arrival directions of the primary particles. The operation of the proposed RPC detector together with the scintillating tracking layers of MATHUSLA would improve the reconstruction of EAS induced by TeV cosmic rays, making possible the exploration of the energy spectrum of cosmic rays at the frontier between direct and indirect cosmic-ray experiments. At the moment, TeV measurements of cosmic rays with EAS detectors are done at high altitudes, but with MATHUSLA they could also be carried out close to sea level. There exists a possibility of including in MATHUSLA simultaneous observations of EAS with the CMS detector. In this case, the CMS-MATHUSLA instrument would provide novel data on the muon content of EAS with energies above 61 GeV that would help to perform tests of high-energy hadronic interaction models and to explore the relation between underground muon bundles and cosmic rays. In conclusion, an experimental detector like MATHUSLA has the potential to address questions in particle physics and high-energy astrophysics.

⁵“During the final stages of this work, the MATHUSLA collaboration added an additional layer of scintillating bars at the top of the detector. After evaluation, we conclude that the additional layer has no effect on the conclusions of this study

Acknowledgments

M.R.C. thankfully acknowledges the permission to use computer resources, the technical advice, and the support provided by the Laboratorio Nacional de Supercómputo del Sureste de México (LNS), a member of the Consejo Nacional de Humanidades, Ciencias y Tecnologías (CONACyT) national network of laboratories, with resources from grant number 201701035C. Financial support for this work has been received from CONAHCyT, grant number A1-S-13525. Also many thanks to the High Performance Computing Laboratory LARCAD-UNACH Mexico, and the Digital Research Alliance of Canada, for the use of the Cedar computing cluster. CA and HJL thank the U. S. National Science Foundation for their support. O.G. Morales-Olivares was supported by a CONACyT postdoctoral fellowship. J.C. Arteaga-Velázquez and D. Rivera thank the support from CONAHCyT, grant number A1-S-46288.

References

- [1] J. P. Chou, D. Curtin, and H. J. Lubatti, *New Detectors to Explore the Lifetime Frontier*, *Phys. Lett.* **B767** (2017) 29–36.
- [2] **MATHUSLA** Collaboration, C. Alpigiani et al., *A Letter of Intent for MATHUSLA: A Dedicated Displaced Vertex Detector above ATLAS or CMS*, *CERN-LHCC-2018-025, LHCC-I-031* (2018) [[arXiv:1811.00927](https://arxiv.org/abs/1811.00927)].
- [3] **MATHUSLA** Collaboration, C. Alpigiani et al., *Recent Progress and Next Steps for the MATHUSLA LLP Detector*, 2022.
- [4] J. Bluemer, R. Engel, and J. R. Hoerandel, *Cosmic rays from the knee to the highest energies*, *Prog. Part. Nucl. Phys.* **63** (2009) 293 – 338.
- [5] I. A. Grenier, J. H. Black, and A. W. Strong, *The Nine Lives of Cosmic Rays in Galaxies*, *Annu. Rev. Astron. Astrophys.* **53** (2015) 199 – 246.
- [6] S. Mollerach and E. Roulet, *Progress in high-energy cosmic ray physics*, *Prog. Part. Nucl. Phys.* **98** (2018) 85 – 118.
- [7] M. Tanabashi et al., *2019 Review of Particle Physics*, *Phys. Rev.* **D 98** (2018) 030001.
- [8] **HAWC** Collaboration, J. Arteaga-Velázquez et al., *Analysis of the composition of TeV cosmic rays with HAWC*, *PoS(ICRC2023)* **299** (2023).
- [9] **KASCADE** Collaboration, T. Antoni et al., *KASCADE measurements of energy spectra for elemental groups of cosmic rays: Results and open problems*, *Astropart. Phys.* **24** (2005) 1.
- [10] **KASCADE-Grande** Collaboration, W. D. Apel, et al., *KASCADE-Grande measurements of energy spectra for elemental groups of cosmic rays*, *Astropart. Phys.* **47** (2013) 54.
- [11] **Pierre Auger** Collaboration, A. Abdul-Halim and et al., *Geometric structures in hadronic cores of extensive air showers observed by cascade*, *J. Cosmol. Astropart. Phys.* **05** (2023) 024.
- [12] B. Peters, *Primary cosmic radiation and extensive air showers*, *Il Nuovo Cimento* **22** (1961) 800.
- [13] G. Giacinti, M. Kachelrieß, and D. V. Semikoz, *Escape model for galactic cosmic rays and an early extragalactic transition*, *Phys. Rev. D* **91** (2015) 083009.

- [14] W. Liu, Y. Q. Guo, and Q. Yuan, *Indication of nearby source signatures of cosmic rays from energy spectra and anisotropies*, *J. Cosmol. Astropart. Phys.* **10** (2019) 010.
- [15] W. Axford, E. Leer, and G. Skadron, *The acceleration of cosmic rays by shock waves*, in *15th International Cosmic Ray Conference (ICRC1977)*, vol. 11 of *International Cosmic Ray Conference*, p. 132, 1977.
- [16] G. Krymsky, *A regular mechanism for the acceleration of charged particles on the front of a shock wave*, *Sov. Phys. Dokl.* **23** (1977) 327.
- [17] A. Bell, *The acceleration of cosmic rays in shock fronts-I*, *Mon. Not. R. Astron. Soc.* **182** (1978) 147.
- [18] R. Blandford, *Particle acceleration by astrophysical shocks*, *Astrophys. J.* **221** (1978) L29.
- [19] O. Deligny, *Cosmic-Ray Anisotropies: A Review*, in *XXV ECRS 2016 Proceedings*, 2016. [arXiv:1612.08002](https://arxiv.org/abs/1612.08002).
- [20] V. Ahlers and P. Mertsch, *Origin of Small-Scale Anisotropies in Galactic Cosmic Rays*, *Prog. Part. and Nucl. Phys.* **94** (2017) 184.
- [21] O. Deligny, *Measurements and implications of cosmic ray anisotropies from TeV to trans-EeV energies*, *Astrop. Phys.* **104** (2019) 13–41.
- [22] V. Ahlers, *The Dipole Anisotropy of Galactic Cosmic Rays*, *J. of Phys. Conf. Series* **1181** (2019) 012004.
- [23] L. Caccianiga, et al., *Update on the searches for anisotropies in UHECR arrival directions with the Pierre Auger Observatory and the Telescope Array*, *PoS(ICRC2023)* **521** (2023).
- [24] **Pierre Auger** Collaboration, A. Aab, et al., *Observation of a Large-scale Anisotropy in the Arrival Directions of Cosmic Rays above 8×10^{18} eV*, *Science* **357** (2017) 1266 – 1270.
- [25] M. Kachelriess and D. Semikoz, *Cosmic ray models*, *Prog. Part. Nuc. Phys.* **109** (2019) 103710.
- [26] M. Kachelriess and D. Semikoz, *Transition from galactic to extragalactic cosmic rays*, *Astropart. Phys.* **39-40** (2012) 129–143.
- [27] **HESS** Collaboration, A. Abramowski, et al., *Acceleration of petaelectronvolt protons in the Galactic Centre*, *Nature* **531** (2016) 476–479.
- [28] **HAWC** Collaboration, A. U. Abeysekara, et al., *HAWC observations of the acceleration of very-high-energy cosmic rays in the Cygnus Cocoon*, *Nature* **5** (2021) 465–471.
- [29] S. Wu, et al., *Highlight of LHAASO science results on PeVatrons*, *PoS(ICRC2023)* **010** (2023).
- [30] G. Golup, et al., *An update on the arrival direction studies made with data from the Pierre Auger Observatory*, *PoS(ICRC2023)* **252** (2023).
- [31] L. S. Collaboration and V. C. et al., *Multi-messenger observations of a binary neutron star merger*, *The Astrophys. J.* **848** (2017), no. 2 L12.
- [32] I. C. et al., *Multiwavelength follow-up of a rare icecube neutrino multiplet*, *Astron. and Astrophys.* **607** (2017) A115.
- [33] R. Engel, D. Heck, and T. Pierog, *Extensive air showers and hadronic interactions at high energy*, *Annual Review of Nuclear and Particle Science* **61** (2011), no. 1 467–489.
- [34] N. Tomassetti, *Direct Measurements of Galactic Cosmic Rays*, [arXiv:2301.10255](https://arxiv.org/abs/2301.10255).

- [35] E. S. Seo, *Direct measurements of cosmic rays using balloon borne experiments*, *Astropart. Phys.* **39** (2012) 76 – 87.
- [36] E. Mocchiutti, *Direct detection of cosmic rays: through a new era of precision measurements of particle fluxes*, *Nucl. Phys. B* **39** (2014) 161 – 172.
- [37] P. Maestro, *Cosmic rays: direct measurements*, in *International Cosmic Ray Conference (ICRC)*, 34th ICRC, October, 2015.
- [38] **AMS** Collaboration, A. Kounine et al., *The Alpha Magnetic Spectrometer on the International Space Station*, *Int. J. Mod. Phys. E* **21** (2012) 1230005.
- [39] **AMS** Collaboration, M. Aguilar et al., *Precision Measurement of the Proton Flux in Primary Cosmic Rays from Rigidity 1 GV to 1.8 TV with the Alpha Magnetic Spectrometer on the International Space Station*, *Phys. Rev. Lett.* **114** (2015) 171103.
- [40] **CREAM** Collaboration, H. S. Ahn et al., *The Cosmic Ray Energetics And Mass (CREAM) instrument*, *Nucl. Instrum. Meth. A* **579** (2017) 1034 – 1053.
- [41] **Fermi-LAT** Collaboration, M. Ackermann et al., *Detection of the Characteristic Pion-Decay Signature in Supernova Remnants*, *Science* **339** (2013) 807–811.
- [42] **KASCADE-Grande** Collaboration, W. D. Apel, et al., *The spectrum of high-energy cosmic rays measured with KASCADE-Grande*, *Astropart. Phys.* **36** (2012) 183–194.
- [43] **IceCube** Collaboration, M. Aartsen et al., *Measurement of the cosmic ray energy spectrum with IceTop-73*, *Phys. Rev. D* **88** (2013) 042004.
- [44] **TUNKA** Collaboration, V. Prosin et al., *Tunka-133: Results of 3 year operation*, *Nucl. Instrum. Meth. A* **756** (2014) 94 – 101.
- [45] M. A. et al., *The Ice Cube Neutrino Observatory*, in *International Cosmic Ray Conference (ICRC)*, 35th ICRC, October, 2017. [arXiv:1710.01207](https://arxiv.org/abs/1710.01207).
- [46] **Telescope Array** Collaboration, T. Abu-Zayyad et al., *The cosmic-ray energy spectrum observed with the surface detector of the Telescope Array Experiment*, *ApJ* **768** (2013) L1.
- [47] **KASCADE** Collaboration, T. Antoni et al., *The cosmic-ray experiment KASCADE*, *Nucl. Instrum. Meth. A* **513** (2003) 490 – 510.
- [48] **TAIGA** Collaboration, N. Budnev et al., *The TAIGA experiment: From cosmic-ray to gamma-ray astronomy in the Tunka valley*, *Nucl. Instrum. Meth. A* **845** (2017) 330 – 333.
- [49] **Tibet AS Gamma** Collaboration, M. Amenomori et al., *First Detection of Photons with Energy beyond 100 TeV from an Astrophysical Source*, *Phys. Rev. Lett.* **123** (2019) 051101.
- [50] **LHAASO** Collaboration, Z. Cao and et al., *Ultrahigh-energy photons up to 1.4 petaelectronvolts from 12 γ -ray galactic sources*, *Nature* **594** (2021) 33.
- [51] **SWGO** Collaboration, A. Albert et al., *Science Case for a Wide Field-of-View Very-High-Energy Gamma-Ray Observatory in the Southern Hemisphere*, [arXiv:1902.08429](https://arxiv.org/abs/1902.08429).
- [52] **ALPACA** Collaboration, C. Calle et al., *A new High Energy Gamma-Ray Observatory in the southern hemisphere*, *J. Phys* **1468** (2020) 012091.
- [53] **LHAASO** Collaboration, G. Di Sciascio et al., *The LHAASO experiment: from Gamma-Ray to Cosmic Rays*, [arXiv:1602.07600](https://arxiv.org/abs/1602.07600).

- [54] A. Olinto and et al., *POEMMA (Probe of Extreme Multi-Messenger Astrophysics) Roadmap Update*, *PoS(ICRC2023)* **1159** (2023).
- [55] **CMS** Collaboration, T. C. Collaboration, *The CMS experiment at the CERN LHC*, *JINST* **3** (2008) S08004–S08004.
- [56] G. Apollinari, O. Bruening, T. Nakamoto, and L. Rossi, *High Luminosity Large Hadron Collider HL-LHC*, *CERN Yellow Report CERN-2015-005* (2015) 1–19.
- [57] **ARGO-YBJ** Collaboration, G. Aielli et al., *Layout and performance of rpcs used in the argo-ybj experiment*, *Nucl. Instrum. Meth. A* **562** (2006), no. 1 92 – 96.
- [58] **ARGO-YBJ** Collaboration, B. Bartoli et al., *The analog resistive plate chamber detector of the argo-ybj experiment*, *Astropart. Phys.* **67** (2015) 47 – 61.
- [59] **ATLAS** Collaboration, T. A. Collaboration, *Atlas - muon spectrometer phase-ii upgrade - technical design report*, *CERN report ATL-TDR-026 LHCC-2017-017* (2017) 101 – 155.
- [60] D. Heck, G. Schatz, T. Thouw, J. Knapp, and J. N. Capdevielle, *CORSIKA: A Monte Carlo code to simulate extensive air showers*, Tech. Rep. FZKA-6019, Forschungszentrum und Universität Karlsruhe, Karlsruhe, 1998.
- [61] A. Ferrari, P. R. Sala, A. Fasso, and J. Ranft, *FLUKA: A multi-particle transport code (Program version 2005)*, *CERN-2005-010*, *SLAC-R-773*, *INFN-TC-05-11*, *CERN-2005-10* (2005).
- [62] T. Böhlen, F. Cerutti, M. Chin, A. Fassò, A. Ferrari, P. Ortega, A. Mairani, P. Sala, G. Smirnov, and V. Vlachoudis, *The fluka code: Developments and challenges for high energy and medical applications*, *Nuclear Data Sheets* **120** (2014) 211 – 214.
- [63] S. Ostapchenko, *Monte Carlo treatment of hadronic interactions in enhanced Pomeron scheme: QGSJET-II model*, *Phys. Rev.* **D83** (2011) 014018.
- [64] S. Ostapchenko, *QGSJET-II: physics, recent improvements, and results for air showers*, *EPJ Web of Conferences* **52** (2013) 02001.
- [65] R. Brun and F. Rademakers, *ROOT - An Object Oriented Data Analysis Framework*, *Nucl. Instrum. Meth.* **A389** (1997) 81–86.
- [66] **ARGO-YBJ** Collaboration, G. Aielli et al., *Calibration of the RPC charge readout in the ARGO-YBJ experiment*, *Nucl. Instrum. Meth. A* **661** (2012) S56–S59.
- [67] P. J. Antsaklis and A. N. Michel, *A.9.3 least squares problem*, in *A Linear Systems Primer*. Springer, Birkhauser, 2007.
- [68] F. James, *MINUIT Function Minimization and Error Analysis: Reference Manual Version 94.1*, *CERN-D-506*, *CERN-D506* (1994).
- [69] **KASCADE** Collaboration, W. D. Apel et al., *Comparison of measured and simulated lateral distributions for electrons and muons with KASCADE*, *Astrop. Phys.* **24** (2006) 467.
- [70] **ARGO-YBJ** Collaboration, B. Bartoli et al., *Absolute-energy-scale calibration of ARGO-YBJ for light primaries in multi-TeV region with the Moon shadow observation*, *Astrop. Phys.* **90** (2017) 20.
- [71] J. Nishimura, *Theory of cascade showers*, in *Handbuch der Physik 46/2* (S. Flugge, ed.). Springer, Berlin, 1967.

- [72] K. Kamata and J. Nishimura, *The Lateral and the Angular Structure Functions of Electron Showers*, *Prog. of Theor. Phys. Supp.* **6** (1958) 93.
- [73] K. Greisen, *The extensive air showers*, in *Prog. Cosmic Ray Physics III* (J. Wilson, ed.). North Holland, Amsterdam, 1956.
- [74] **ARGO-YBJ** Collaboration, B. Bartoli et al., *EAS age determination from the study of the lateral distribution of charged particles near the shower axis with the ARGO-YBJ experiment*, *Astrop. Phys.* **93** (2017) 46.
- [75] A. G. Bogdanov, *Intensity of muon bundles according to the NEVOD-DECOR cosmic ray experiment*, *J. Phys.: Conf. Ser.* **1690** (2020) 012007.
- [76] T. Pierog, I. Karpenko, J. M. Katzy, E. Yatsenko, and K. Werner, *Epos lhc: Test of collective hadronization with data measured at the cern large hadron collider*, *Phys. Rev. C* **92** (Sep, 2015).
- [77] F. Riehn, H. Dembinski, R. Engel, A. Fedynitch, T. K. Gaisser, and T. Stanev, *The hadronic interaction model Sibyll 2.3c and Feynman scaling*, in *35th International Cosmic Ray Conference (ICRC2017)*, vol. 301 of *International Cosmic Ray Conference*, p. 301, 2017. [arXiv:1709.07227](https://arxiv.org/abs/1709.07227).
- [78] L. Cazon et al., *Working Group Report on the Combined Analysis of Muon Density Measurements from Eight Air Shower Experiments*, *PoS(ICRC2019)* **214** (2019).
- [79] H. P. Dembinski et al., *Data-driven model of the cosmic-ray flux and mass composition from 10 GeV to 10^{11} GeV*, *PoS(ICRC2017)* **533** (2017).
- [80] P. Lipari and T. Stanev, *Propagation of multi-teV muons*, *Phys. Rev. D* **44** (1991) 3543–3554.
- [81] CMS, *Performance of CMS muon reconstruction in cosmic-ray events*, *Journal of Instrumentation* **5** (2010), no. 03 T03022–T03022.
- [82] L. Sonnenschein and et al., *CMS: Cosmic muons in simulation and measured data- Drift velocity monitoring of the CMS muon drift chambers*, *PoS(HCP2009)* **098** (2009).
- [83] G. Anzivino and et al., *Single and multiple muon events in the lvd detector*, *Nucl. Instrum. Meth. A* **295** (1990), no. 3 466–476.
- [84] **Fréjus** Collaboration, C. Berger, et al., *Experimental study of muon bundles observed in the fréjus detector*, *Phys. Rev. D* **40** (1989) 2163–2171.
- [85] **MACRO** Collaboration, M. Ambrosio, et al., *High energy cosmic ray physics with underground muons in macro. i. analysis methods and experimental results*, *Phys. Rev. D* **56** (1997) 1407–1417.
- [86] **ALEPH** Collaboration, K. Gruppen et al., *Measurements of the muon component of extensive air showers at 320 m.w.e. underground*, *Nucl. Instrum. Meth. A* **510** (2003) 190.
- [87] **L3+C** Collaboration, O. Adriani, et al., *The l3+c detector, a unique tool-set to study cosmic rays*, *Nucl. Instrum. Meth. A* **488** (2002), no. 1 209–225.
- [88] **DELPHI** Collaboration, J. Ridky et al., *Detection of muon bundles from cosmic ray showers by the DELPHI experiment*, *Phys. Proc. Suppl. B* **138** (2005) 295–298.
- [89] P. Travineck, *Detection of cosmic ray events by LEP experiments*, *Czech. J. of Phys.* (2006) A185–A200.
- [90] N. Kalmykov, S. Ostapchenko, and A. Pavlov, *Quark-gluon-string model and eas simulation problems at ultra-high energies*, *Nucl. Phys. B - Proc. Suppl.* **52** (1997), no. 3 17–28.

- [91] **ALICE** Collaboration, J. Adam et al., *Study of cosmic ray events with high muon multiplicity using the ALICE detector at the CERN Large Hadron Collider*, *JCAP* **01** (2016) 032.
- [92] **ALICE** Collaboration, K. Aamodt et al., *The ALICE experiment at the CERN LHC*, *JINST* **3** (2008) S08002.
- [93] **ALICE** Collaboration, M. Rodríguez Cahuantzi et al., *Cosmic-ray physics at CERN*, *J.Phys.Conf.Ser.* **866** (2017) 012013.
- [94] E. Farhi and R. L. Jaffe, *Strange matter*, *Phys. Rev. D* **30** (1984) 2379.
- [95] P. Kankiewicz et al., *Muon bundles as a sign of strangelets from the Universe*, *Astrophys. J.* **839** (2017) 31.
- [96] M. Rybczynski and Z. Włodarczyk, *Can strangelets solve the muon puzzle?*, *EPJ Web of Conferences* **208** (2019) 04004.
- [97] **PAO** Collaboration, A. Aab, et al., *Reconstruction of inclined air showers detected with the Pierre Auger Observatory*, *JCAP* **08** (2014) 019.
- [98] J. Wrotniak, *SHOWERSIM/84*, University of Maryland, *UMCP Report PP85-191 (1985)* (1985).
- [99] **KASCADE** Collaboration, T. Antoni et al., *Search for cosmic ray point sources with KASCADE*, *Astrophys. J.* **608** (2004) 865–871.
- [100] D. Kang and et al., *Search for gamma-ray point sources with KASCADE*, *PoS(ICRC2015)* **812** (2015).
- [101] M. Pohl and D. Eichler, *UNDERSTANDING TeV-BAND COSMIC-RAY ANISOTROPY*, *The Astrophys. J.* **766** (2013) 4.
- [102] X. M. et al., *Study on Multicore Extensive Air Showers in the ARGO-YBJ Experiment*, in *International Cosmic Ray Conference (ICRC)*, 31st ICRC, July, 2009.
- [103] X. M. e. a. J. Zhao, *Multicore cosmic shower in the ARGO-YBJ experiment*, in *International Cosmic Ray Conference (ICRC)*, 32nd ICRC, August, 2011.
- [104] **ICECUBE** Collaboration, M. G. Aartsen et al., *Cosmic Ray Spectrum and Composition from PeV to EeV Using 3 Years of Data From IceTop and IceCube*, *Phys. Rev. D* **100** (2019) 082002.
- [105] **ARGO-YBJ** Collaboration, B. Bartoli et al., *Cosmic ray proton plus helium energy spectrum measured by the ARGO-YBJ experiment in the energy range 3–300 TeV*, *Phys. Rev. D* **91** (2015) 112017.
- [106] T. K. Gaisser, T. Stanev, and S. Tilav, *Cosmic ray energy spectrum from measurements of air showers*, *Front. of Phys.* **8** (2013) 748.
- [107] J. R. Hörandel, *Models of the knee in the energy spectrum of cosmic rays*, *Astropart. Phys.* **21** (2004) 241–265.
- [108] C. Alcock, E. Farhi, and A. Olinto, *Strange Stars*, *Astrophys. J.* **310** (1986) 261–272.
- [109] K. S. Cheng and V. V. Usov, *Strangelets accelerated by pulsars in galactic cosmic rays*, *Phys. Rev. D* **74** (2006) 127303.
- [110] J. Pinfold and et al., *A proposal for the ATLAS cosmic muon and exotics detector (ACME) at the LHC*, in *Astroparticle, Particle, Space Physics and Detectors for Physics Applications*, Proceedings of the 13th ICATPP Conference, Villa Olmo, Como, Italy, 3 – 7 October 2011, September, 2012.
- [111] **LHAASO** Collaboration, X. Bai et al., *The Large High Altitude Air Shower Observatory (LHAASO) Science White Paper*, *Chinese Phys. C* **46** (2022), no. 3 035001–035007, [[arXiv:1905.02773](https://arxiv.org/abs/1905.02773)].

- [112] **HAWC** Collaboration, R. Alfaro et al., *All-particle cosmic ray energy spectrum measured by the HAWC experiment from 10 to 500 TeV*, *Phys. Rev. D* **96** (2017) 122001.
- [113] **ICECUBE** Collaboration, R. Abbasi et al., *IceTop: The surface component of IceCube*, *Nucl. Instr. and Meth. A* **700** (2013) 188.
- [114] **ICECUBE** Collaboration, R. Koirala et al., *Low Energy Cosmic Ray Spectrum from 250 TeV to 10 PeV using IceTop*, *PoS(ICRC2019)* **318** (2019).
- [115] **Telescope array** Collaboration, S. Ogio et al., *Telescope array Low energy Extension*, *JPS Conf. Proc.* **19** (2018) 011026.
- [116] **Telescope array** Collaboration, R. U. Abbasi et al., *The Cosmic-Ray Energy Spectrum between 2 PeV and 2 EeV Observed with the TALE detector in monocular mode*, *Astrophys. J.* **865** (2018) 74.
- [117] **Telescope array** Collaboration, S. Ogio et al., *Telescope Array Experiment*, *EPJ Web of Conferences* **208** (2019) 08002.
- [118] **ARGO-YBJ** Collaboration, B. Bartoli et al., *Knee of the cosmic hydrogen and helium spectrum below 1 PeV measured by ARGO-YBJ and a Cherenkov telescope of LHAASO*, *Phys. Rev. D* **92** (2015) 092005.
- [119] **KASCADE** Collaboration, T. Antoni et al., *The Cosmic-Ray Experiment KASCADE*, *Nucl. Instr. and Meth. A* **513** (2003) 490.
- [120] **KASCADE** Collaboration, P. Doll et al., *Muon tracking detector for the air shower experiment KASCADE*, *Nucl. Instr. and Meth. A* **488** (2002) 517.
- [121] **TAIGA** Collaboration, V. V. Prosin et al., *Energy Spectrum of Primary Cosmic Rays, According to TUNKA-133 and TAIGA-HiSCORE EAS Cherenkov Light Data*, *Bull. Russ. Acad. Sci. Phys.* **83** (2019) 1016.
- [122] **TAIGA** Collaboration, M. Tluczykont et al., *TAIGA-HiSCORE: results from the first two operation seasons*, *PoS(ICRC2017)* **759** (2018).
- [123] **GAMMA** Collaboration, A. Garyaka, et al., *Rigidity-dependent cosmic ray energy spectra in the knee region obtained with the GAMMA experiment*, *Astropart. Phys.* **28** (2007) 169.
- [124] **LHAASO** Collaboration, H. Zhang and et al., *Measurement of muon contents in cosmic ray shower with LHAASO-KM2A around knee region*, *PoS(ICRC2021)* **352** (2021).
- [125] **ICECUBE** Collaboration, D. Soldin and et al., *Density of GeV Muons Measured with IceTop*, *PoS(ICRC2021)* **342** (2021).
- [126] **EMMA** Collaboration, P. Kuusiniemi and et al., *Performance of tracking stations of the underground cosmic-ray detector array emma*, *Astropart. Phys.* **102** (2018) 67–76.
- [127] **EMMA** Collaboration, W.H. Trzaska et al., *Possibilities for Underground Physics in the Pyhasalmi mine*, [arXiv:1810.00909](https://arxiv.org/abs/1810.00909).
- [128] **EMMA** Collaboration, W. H. Trzaska and et al., *High-multiplicity muon events observed with EMMA array*, *J. Phys. Conf. Ser.* **1468** (2020), no. 1 012085.
- [129] S. Over and et al., *Search for anisotropy and point sources of cosmic rays with the KASCADE-Grandeexperiment*, *Proc. of the 30th ICRC, Mérida, Mexico* **4(HE-1)** (2008) 223.

- [130] **KASCADE-Grande** Collaboration, W. D. Apel and et al., *Lateral distributions of eas muons ($e_{\mu} > 800$ mev) measured with the kascade-grande muon tracking detector in the primary energy range 10^{16} – 10^{17} ev*, *Astropart. Phys.* **65** (2015) 55–63.
- [131] **KASCADE-Grande** Collaboration, W. D. Apel and et al., *Muon production height studies with the air shower experiment kascade-grande*, *Astropart. Phys.* **34** (2011), no. 6 476.
- [132] **KASCADE-Grande** Collaboration, W. D. Apel and et al., *Test of interaction models up to 40 PeV by studying hadronic cores of EAS*, *Journal of Physics G: Nuclear and Particle Physics* **34** (2007), no. 12 2581.
- [133] **KASCADE** Collaboration, T. Antoni and et al., *Geometric structures in hadronic cores of extensive air showers observed by kascade*, *Phys. Rev. D* **71** (2005) 072002.
- [134] **KASCADE** Collaboration, T. Antoni and et al., *Test of hadronic interaction models in the forward region with kascade event rates*, *Journal of Physics G: Nuclear and Particle Physics* **27** (2001), no. 8 1785.
- [135] **KASCADE** Collaboration, T. Antoni and et al., *Test of high-energy interaction models using the hadronic core of eas*, *Journal of Physics G: Nuclear and Particle Physics* **25** (1999), no. 10 2161.
- [136] **KASCADE** Collaboration, O. Saavedra and et al., *NEVOD-DECOR experiment: results and future*, *J. Phys. Conf. Ser.* **409** (2013) 012009.
- [137] **NEVOD-DECOR** Collaboration, E. Yurina and et al., *Measurements of the average muon energy in inclined muon bundles in the NEVOD-DECOR experiment*, *PoS(ICRC2021)* **383** (2021).
- [138] **LHAASO** Collaboration, F. Aharonian, et al., *The observation of the Crab Nebula with LHAASO-KM2A for the performance study*, *Chinese Phys. C* **45** (2021) 025002.